nature climate change

Article

https://doi.org/10.1038/s41558-025-02375-1

Contrasting biological production trends over land and ocean

Received: 18 December 2024

Accepted: 10 June 2025

Published online: 1 August 2025

Check for updates

Yulong Zhang[1,2,3] ✉, Wenhong Li[1], Ge Sun[2], Jiafu Mao[3], Matthew Dannenberg[4], Jingfeng Xiao[5], Zuchuan Li[1,6], Haipeng Zhao[1], Qianru Zhang[1], Shineng Hu[1], Conghe Song[7] & Nicolas Cassar[1] ✉

Terrestrial and marine ecosystems constitute the primary components of the Earth's biosphere, yet their photosynthetic productions are typically studied separately, which limits understanding of planetary carbon uptake and biosphere health. Here, using multiple satellite-derived products, we identify contrasting net primary production (NPP) trends between land and ocean, probably reflecting their differential sensitivity to climate warming, especially in tropical regions. Planetary NPP shows an overall increase of 0.11 ± 0.13 PgC yr^{-1} ($P = 0.05$) from 2003 to 2021, driven by a significant terrestrial enhancement of 0.20 ± 0.07 PgC yr^{-1} ($P < 0.001$) and partially offset by an oceanic decline of -0.12 ± 0.12 PgC yr^{-1} ($P = 0.07$). While land contributes to the strong upwards NPP trend, the interannual variability in global NPP is predominantly driven by the ocean, especially during strong El Niño–Southern Oscillation events. Our findings highlight the resilience and potential vulnerability of biosphere primary productivity in a warming climate, calling for integrated land–ocean monitoring and assessment to support climate mitigation initiatives.

The biosphere is fundamental to the regulation of global biogeochemical cycles and the preservation of Earth's habitability[1]. At the core of this system lies the net primary production (NPP), a biological process where autotrophic organisms, such as terrestrial plants and marine phytoplankton, convert atmospheric carbon dioxide into organic matter through photosynthesis, after accounting for carbon losses from autotrophic respiration[2]. NPP represents the net accumulation of energy that sustains growth, reproduction and consumption by heterotrophs within an ecosystem. This essential process forms the base of food webs[3] and serves as a key driver of global carbon sink[4,5] that contributes to mitigating anthropogenic carbon emissions and stabilizing Earth's climate[6].

While terrestrial and oceanic ecosystems share the fundamental biochemical mechanism of photosynthesis, their NPP dynamics diverge due to distinct biological communities and environmental constrains[2,7,8]. Previous research reported a drought-induced decline in global terrestrial NPP from 2000 to 2009[9]. Subsequent studies, however, indicated a reversal of this trend due to climate warming, CO_2 fertilization and afforestation, particularly in northern mid and high latitudes[5,10–12]. Nonetheless, more recent research has suggested a slowdown in the increase of global land gross carbon uptake due to the enhanced atmospheric aridity[13–15]. By contrast, marine NPP experienced a significant rise during the El Niño–La Niña transition from 1997 to 1999, followed by a sharp decline by 2006, probably due to reduced upwelling and nutrient supply caused by ocean warming[7,16]. Recent evaluations using multiple marine models confirmed the continuation of this downwards trend through approximately 2020 (refs. 17–19), though with notable uncertainty[19,20]. Despite considerable advancements

[1]Division of Earth and Climate Sciences, Nicholas School of the Environment, Duke University, Durham, NC, USA. [2]Eastern Forest Environmental Threat Assessment Center, Southern Research Station, USDA Forest Service, Raleigh, NC, USA. [3]Environmental Sciences Division, Oak Ridge National Laboratory, Oak Ridge, TN, USA. [4]School of Earth, Environment, and Sustainability, University of Iowa, Iowa City, IA, USA. [5]Earth Systems Research Center, Institute for the Study of Earth, Oceans, and Space, University of New Hampshire, Durham, NH, USA. [6]Data and Environmental Sciences, Duke Kunshan University, Kushan, China. [7]Department of Geography and Environment, University of North Carolina at Chapel Hill, Chapel Hill, NC, USA.
✉e-mail: yulong.zhang@duke.edu; nicolas.cassar@duke.edu

in assessing global primary productivity within terrestrial[21–24] and marine[17,25,26] ecosystems independently, efforts to explore these two systems simultaneously in a cohesive manner have been insufficient. This is largely due to challenges in harmonizing disparate measurement techniques, spatial and temporal scales and modelling approaches[27–29], leaving a significant gap in understanding biospheric carbon uptake as a unified planetary process[8]. Notably, it has been over two decades since pioneering integrated studies of land and ocean primary productivity[2,7], highlighting the pressing need to revisit this frontier and advance a comprehensive, planetary-scale understanding of contemporary global NPP dynamics.

The National Aeronautics and Space Administration (NASA) Earth Observing System programme has provided continuous measurements and advanced modelling capacities of the Earth's surface since the early 2000s[30,31], offering a unique opportunity to examine biological primary production across terrestrial and marine environments. Here, we investigate long-term trends and variability in global NPP from 2003 to 2021 using multiple satellite-derived land and ocean NPP products. We aim to explore the patterns and putative drivers of contemporary global NPP dynamics, with a particular focus on potential synergies and trade-offs between terrestrial and marine ecosystems. By addressing these questions, our biosphere-scale assessment could provide critical insights from an integrated land–ocean perspective to support the preservation of global ecosystem services and inform effective strategies for climate mitigation and adaptation on a warming planet.

Contrasting land and ocean NPP trends

We identify diverging annual NPP trends over land and ocean from 2003 to 2021 based on the ensemble means from three remote sensing (RS)-based land NPP products (Moderate Resolution Imaging Spectroradiometer (MOD17), Global Land Surface Satellite (GLASS) and Boreal Ecosystem Productivity Simulator (BEPS)) and three ocean NPP products (the Eppley-Vertically Generalized Production model (EVGPM), the Carbon-based Production model (CbPM) and the Carbon, Absorption and Fluorescence Euphotic-resolving model (CAFE)) (Fig. 1, Methods and Extended Data Fig. 1). Specifically, land NPP exhibits a strong upwards trend at a rate of 0.20 ± 0.07 PgC yr^{-1} ($P < 0.001$) according to the Theil–Sen regression with Mann–Kendal significance testing (hereafter the same) (Fig. 1a). By contrast, ocean NPP shows a weaker declining trend of −0.12 ± 0.12 PgC yr^{-1} ($P = 0.07$) (Fig. 1b). Consequently, the global NPP trend is dominated by land NPP, yielding a net increase of 0.11 ± 0.13 PgC yr^{-1} ($P = 0.05$; Fig. 1c). Trends estimated using ordinary least squares linear regression are comparable to those obtained using Theil–Sen regression, exhibiting similar amplitudes across global, terrestrial and marine domains (Fig. 1d).

We note a trend shift for ocean NPP in 2015 (Fig. 1b) using segmented regression analysis (Methods). Following this year, ocean NPP exhibits a marked reversal from a significant decline (−0.23 PgC yr^{-1}; $P < 0.001$) to a strong increase (0.39 PgC yr^{-1}; $P = 0.01$), primarily concentrated in mid- and high-latitude oceans (Extended Data Fig. 2). By contrast, no similar change point is observed for the land NPP trend (Fig. 1a). Consequently, global NPP transitions from an nonsignificant decrease before 2015 (−0.06 PgC yr^{-1}; $P = 0.59$) to a significant increase thereafter (0.59 PgC yr^{-1}; $P = 0.002$) (Fig. 1c). Overall, annual land and ocean NPP dynamics are generally consistent with changes in vegetation greenness and phytoplanton adundance, as reflected by leaf area index (LAI) ($R^2 = 0.92$, $P < 0.001$; Fig. 1a) and ocean chlorophyll concentration (CHL) ($R^2 = 0.60$, $P = 0.007$; Fig. 1b), respectively.

Global ensembles of process-based models, including Dynamic Global Vegetation Models (DGVMs) for terrestrial ecosystems and Global Ocean Biogeochemistry Models (GOBMs) for marine ecosystems (Methods), generally capture the direction of land and ocean NPP trends reflected by RS-based models (Fig. 1e,f). However, both DGVM and GOBM ensembles tend to underestimate the magnitude of NPP trends compared with RS-based estimates (Fig. 1e,f). Moreover, despite substantial variability among individual models, the GOBM ensemble mean exhibits notably lower interannual variability relative to RS-based ocean models (Extended Data Fig. 3). This discrepancy suggests that current process-based models may inadequately represent short-term environmental variations reflected by RS-based models[19], highlighting the need for improved data–model integration to enhance global NPP simulations[32].

Spatial variability of land and ocean NPP trends

Despite the notable difference in surface area (23.7% land versus 76.3% ocean), land and ocean contribute comparable amounts to global NPP, at 55.8 ± 2.1 PgC yr^{-1} and 51.9 ± 3.3 PgC yr^{-1}, respectively (Extended Data Fig. 1a). Latitudinally, both accumulated land and ocean NPP peak in the tropics and decline towards the poles (Fig. 2a). However, land NPP exhibits an asymmetric distribution with a secondary peak in the northern mid-latitudes (~53° N), while ocean NPP shows a secondary peak in the southern mid-latitudes (~40° S) (Fig. 2b). These complementary patterns produce a roughly symmetrical global NPP distribution, characterized by subpeaks in both hemispheres. Notably, ocean NPP dominates the global NPP over 44.3% of the latitudinal band area, primarily between 8° and 20° N and south of 20° S (Fig. 2b).

During the study period, land NPP increases significantly ($P \leq 0.05$) across 31.9% of vegetated areas, while only 3.3% of the area experiences significant declines (Fig. 2c,d). By contrast, ocean NPP shows significant increases over only 5.0% of marine areas, while declines affect 18.5%. In absolute terms, the area experiencing significant ocean NPP decline (~64.9 million km^2) is nearly twice that of significant land NPP increase (~34.8 million km^2). Spatially, land NPP gains are widespread across most climate zones, except for tropical America. By contrast, ocean NPP losses are concentrated in extensive tropical and subtropical regions, particularly across the Pacific Ocean (Fig. 2e and Extended Data Fig. 4). Along the latitudinal gradient, global NPP increases are primarily observed north of 20° N, largely driven by land, and south of 15° S, where land and ocean contributions are nearly equal (Fig. 2f). However, substantial declines in ocean NPP outweigh moderate increases on land, leading to a net decline in global NPP across the latitudinal bands between 20° N and 15° S (Fig. 2f).

Global NPP trends are closely linked to baseline productivity, with increases mainly occurring in regions with relatively low to moderate NPP, below 800 gC m^{-2} yr^{-1} on land and 70 gC m^{-2} yr^{-1} in oceans (Fig. 2g,h). On land, boreal and alpine zones, with moderate baseline NPP (403.6 gC m^{-2} yr^{-1}), contribute the most to the global NPP increase (0.08 PgC yr^{-1}; $P < 0.01$) (Extended Data Fig. 4). By contrast, tropical zones, despite their much higher baseline NPP (820.0 gC m^{-2} yr^{-1}), have a limited contribution to the global increase (0.04 PgC yr^{-1}; $P < 0.01$), with even the most productive areas, such as tropical America (936.4 gC m^{-2} yr^{-1}), showing a negligible contribution. In the oceans, tropical waters (baseline NPP of 157.5 gC m^{-2} yr^{-1}) contribute negatively to the global NPP trend (−0.12 PgC yr^{-1}; $P = 0.001$), while cold, high-latitude oceans (baseline NPP of 46.8 gC m^{-2} yr^{-1}) show a small but significant positive trend (0.009 PgC yr^{-1}; $P = 0.04$) (Extended Data Fig. 4).

Environmental controls on land and ocean NPP trends

Annual land and ocean NPP trends exhibit distinct putative environmental controls (Fig. 3). On land, NPP increases are primarily associated with changes in air temperature (TA), accounting for 37.6% of the total significant change area ($P \leq 0.05$), followed by photosynthetically active radiation (PAR) at 28.9% and precipitation (PRE) at 24.0% (Fig. 3a–c). Spatially, warming-associated NPP increases are most prominent in boreal and alpine regions and parts of the temperate zone (Fig. 3a,b and Supplementary Fig. 1). PAR-associated increases dominate in temperate and tropical regions, while PRE-associated gains are concentrated in semi-arid and temperate areas (Fig. 3a,b and Supplementary

https://doi.org/10.1038/s41558-025-02375-1

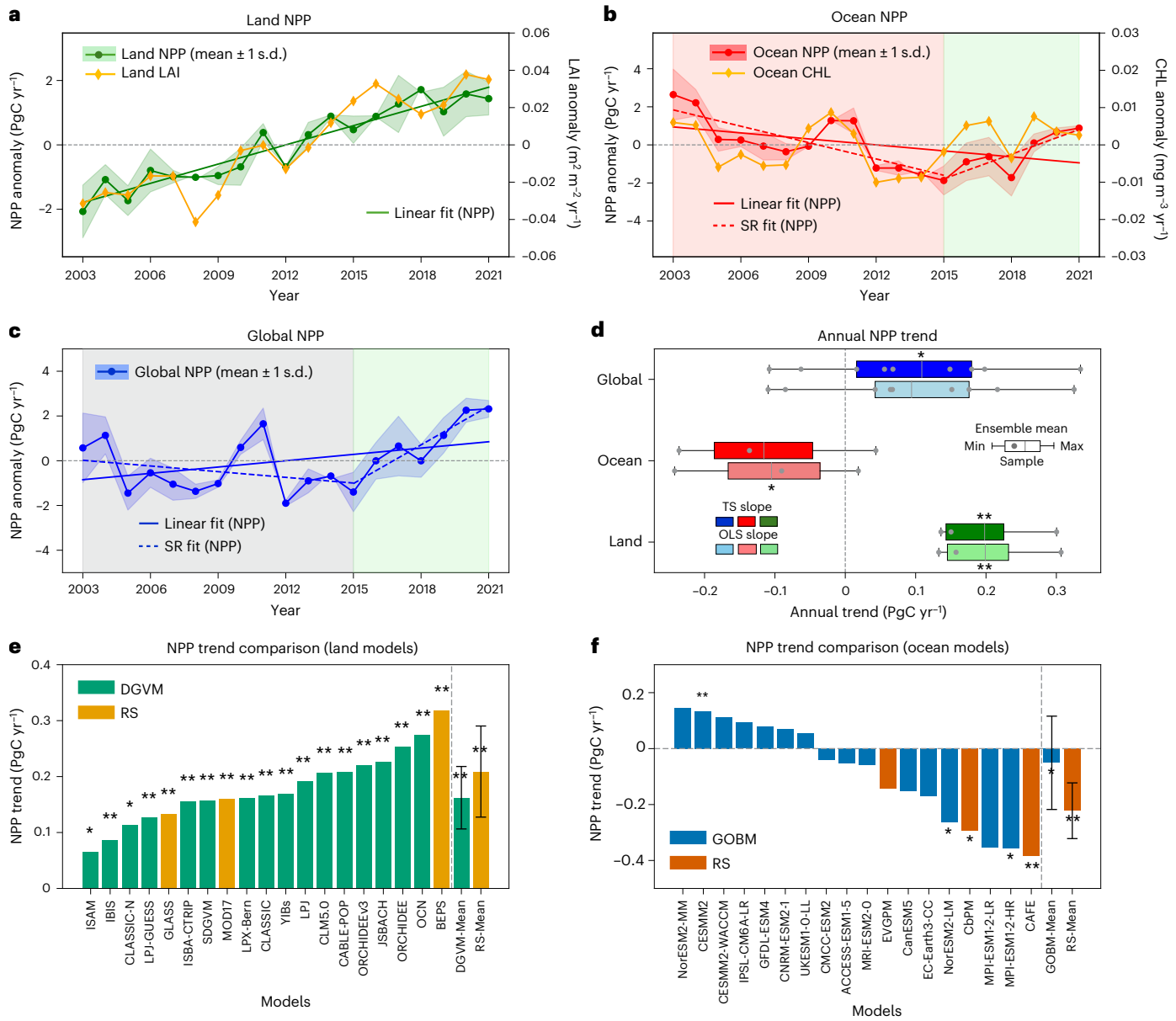

Fig. 1 | Annual NPP changes over land and ocean from 2003 to 2021. a, Annual changes in land NPP (green) and vegetation greenness (yellow), represented by the MODIS LAI. The green shaded area indicates one s.d. across three land NPP products. **b**, Annual changes in ocean NPP (red) and ocean colour (yellow), based on MODIS CHL. The red shaded area represents one s.d. across three ocean NPP products. **c**, Global NPP change (blue), with the blue shaded area indicating one s.d. across nine global NPP combinations. In **a**–**c**, the solid lines represent trends derived from Theil–Sen regression and dotted lines indicate the segmented regressions (SR) when a statistically significant change point is detected. The shaded grey area denotes the period with nonsignificant trends ($P > 0.05$) and the coloured shaded area denotes the period with statistically significant trends ($P \leq 0.05$) based on the Mann–Kendall test. In **b**, the light red area indicates the period with a significant decreasing NPP trend, while the light green area indicates the period with a significant increasing trend. The vertical dotted lines in **b** and **c** mark the detected change point year. No breakpoint is detected in land NPP trends (**a**); therefore, no background colour is shown. **d**, A comparison of annual NPP trends for land, ocean and the globe. The box plots represent Theil–Sen (TS) slope estimates (darker colours) and ordinary least squares (OLS) trends (lighter colours). The vertical grey lines represent annual trends in the ensemble mean of NPP series shown in **a**–**c**. **e**, A comparison of land NPP trends from 16 DGVMs (Methods) and three RS-based models over the overlapping period (2003–2020). DGVM-mean and RS-mean represent the ensemble means of each group, with error bars indicating their s.d. **f**, A comparison of ocean NPP trends from 15 GOBMs (Methods) and three RS-based models over the overlapping period (2003–2014). GOBM-mean and RS-mean denote the ensemble means, with error bars showing s.d. Annual NPP changes from individual models seen in **e** and **f** are shown in Extended Data Fig. 3. In **d**–**f**, significance levels are based on the Mann–Kendall test: $^{*}P \leq 0.05$ and $^{**}P \leq 0.01$.

Fig. 1). However, NPP declines in regions such as the Amazon and parts of Africa are primarily linked to warming-induced atmospheric drying (Extended Data Fig. 6). Although vegetation autotrophic respiration (AR) can be enhanced by climate warming[9], thus potentially reducing NPP, its offsetting effect is secondary compared with total photosynthesis (measured as gross primary production, or GPP). Globally, only 17.5% of NPP change areas are AR dominated, compared with 82.5% driven by GPP (Methods and Extended Data Fig. 6a,b). Nevertheless, warming-associated increases in AR compound GPP decline in some tropical regions, further intensifying observed reductions in NPP (Extended Data Fig. 6a,c,d).

Significant ocean NPP trends ($P \leq 0.05$) are primary linked with changes in sea surface temperature (SST), accounting for 45.3% of total significant change area, followed by mixed-layer depth (MLD; 34.6%)

https://doi.org/10.1038/s41558-025-02375-1

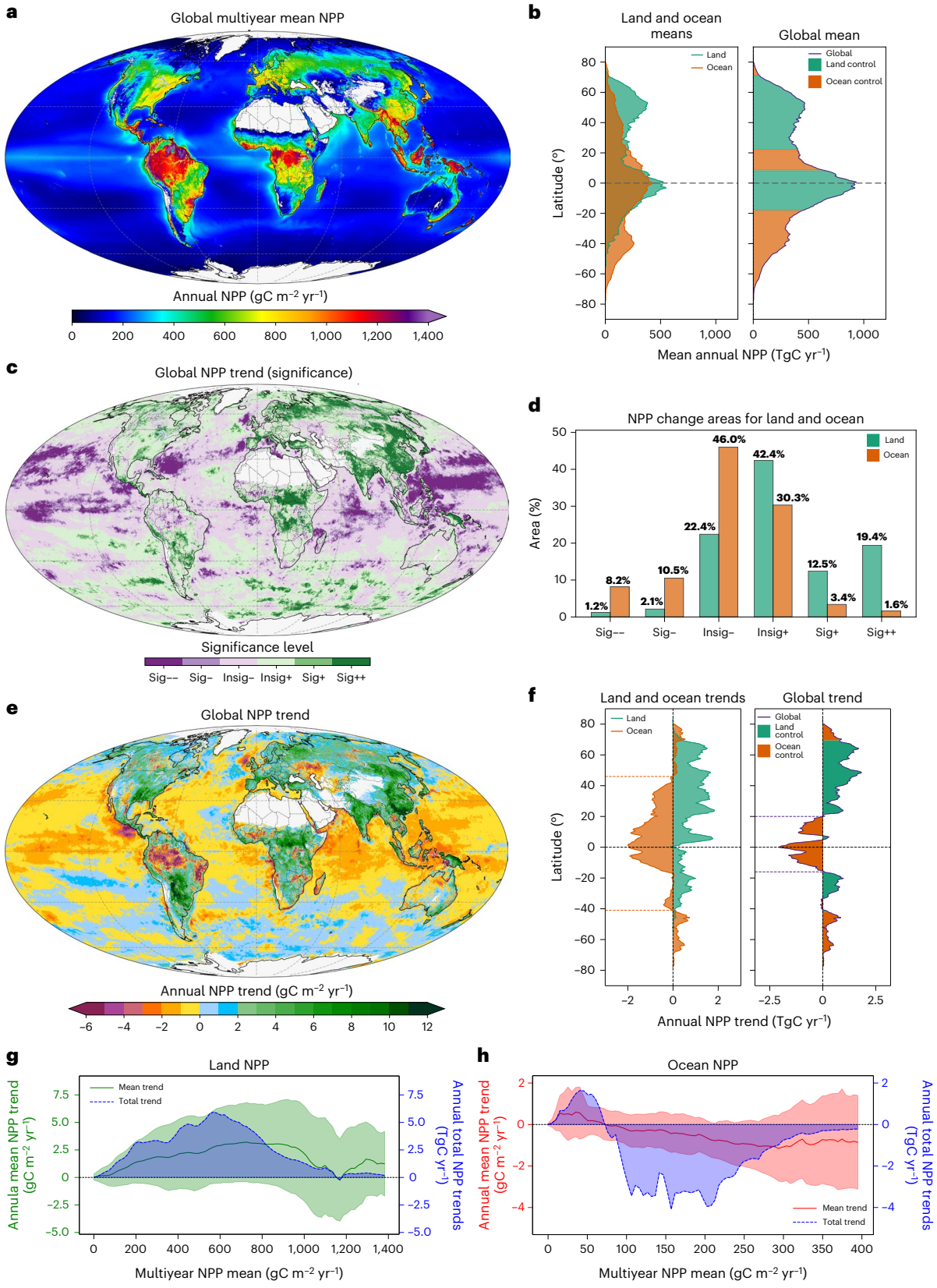

and PAR (20.1%) (Fig. 3d–f). Different from terrestrial ecosystems, ocean NPP shows a much larger proportion of negative temperature association (41.3%) than positive temperature association (4.0%) (Fig. 3a–f). In tropical oceans, NPP declines are primarily linked to increased SST and secondarily with reduced MLD (Fig. 3d–f). Conversely, NPP increases in high-latitude (Southern and Arctic) and southern mid-latitude oceans, probably driven by increased surface PAR and shallower MLD—both enhancing light availability—and by warmer temperatures that potentially ease thermal limitations (Fig. 3d,e and Supplementary Fig. 2).

To further examine the drivers of NPP dynamics, we apply structural equation modelling (SEM) to evaluate the relative contributions

Fig. 2 | Spatial distributions of global NPP mean and trend from 2003 to 2021. a, The multiyear mean NPP for land and ocean (2003–2021). **b**, Latitudinal gradients (0.5° intervals) of area-weighted multiyear mean NPP values for land and ocean (left) and global totals (right). **c**, Spatial patterns of statistical significance for global land and ocean NPP trends. **d**, Summary statistics of trend significance levels for global land and ocean NPP. Significance levels are determined using the Mann–Kendall test: Sig−−, extremely significant negative trend ($P \leq 0.01$); Sig−, significant negative trend ($P \leq 0.05$); Insig−, nonsignificant negative trend ($P > 0.05$); Sig++, extremely significant positive trend ($P \leq 0.01$); Sig+, significant positive trend ($P \leq 0.05$); Insig+, nonsignificant positive trend ($P > 0.05$). In **d**, the area statistics for land and ocean are expressed relative to the total vegetated land area and the total ice-free ocean area, respectively. **e**, Annual NPP trends for land and ocean from 2003 to 2021. **f**, Latitudinal gradients (0.5° intervals) of area-weighted annual NPP trends for land and ocean (left) and global totals (right). The horizontal dashed lines mark zones with negative ocean NPP trends (deep orange) and global NPP trends (dark purple). **g**, Gradient changes in annual NPP trends (shown in **a**) along the multiyear mean land NPP (shown in **e**). Two forms of annual trends are shown: unit-area means (solid green line) and total area-weighted trends (dotted blue line). The shaded green area indicates ±1 s.d. of mean NPP within each mean interval. **h**, Gradient changes in annual NPP trends (shown in **a**) along the multiyear mean ocean NPP (shown in **e**). Two forms of annual trends are shown: unit-area means (solid green line) and total area-weighted trends (dotted blue line). The shaded green area indicates ±1 s.d. of the mean NPP within each mean interval.

of key environmental factors (Methods). While SEM does not establish causation, it reveals statistically supported associations within a hypothesized framework. Overall, the contrasting sensitivity of land and ocean NPP to temperature is further supported by the SEM results (Fig. 3g,h). For land NPP, we observe a strong positive association with annual TA: a 1 s.d. increase in temperature corresponds to a 0.76 unit increase in NPP (Fig. 3g). To account for vegetation structure, we introduce a latent variable, LAI, to reflect the combined influences such as land use/cover change, CO_2 fertilization and nutrient deposition[11]. The results indicate that temperature is positively linked with LAI, which in turn enhances NPP, a consistent pattern across all climate zones (Fig. 3g and Extended Data Fig. 7). However, in tropical regions, temperature exhibits a significant negative direct effect on NPP ($P < 0.05$), probably due to warming-induced water stress and elevated autotrophic respiration (Extended Data Figs. 6 and 7a).

By contrast, global marine SEM analysis shows a strong negative association of SST with ocean NPP, with a 1 s.d. increase in SST linked to a 1.12 unit decrease in ocean NPP (Fig. 3h). To better understand this relationship, we incorporate CHL as a proxy for phytoplankton biomass, and MLD-integrated PAR (MPAR) to represent underwater light availability (Methods). These additions further support the putative negative sensitivity of ocean NPP to rising SST (Fig. 3h). SST is also negatively associated with MLD, particularly in tropical and subtropical regions (Extended Data Fig. 8). In these waters, MLD is positively associated with CHL and subsequently with NPP, suggesting that warming-induced shoaling of the MLD may limit NPP by reducing nutrient availability. Conversely, regions such as the Arctic Ocean, Southern Ocean and shelf waters exhibit positive associations between MPAR and NPP (Extended Data Fig. 8c–e), highlighting the critical role of light availability in supporting productivity in these typically light-limited environments.

ENSO-driven variability in land and ocean NPP

Although it has only a limited contribution to the global NPP trend (Fig. 1), ocean NPP overwhelmingly drives the interannual variability in global detrended NPP ($R^2 = 90\%$, $P < 0.001$), far surpassing the influence of land NPP ($R^2 = 7\%$, $P = 0.28$; Fig. 4a). This interannual variability in both ocean and land NPP are primarily driven by tropical regions (Extended Data Fig. 9 and Supplementary Fig. 3), with tropical ocean NPP dominating in 14 of 19 years and tropical land dominating in 10 of 19 years throughout the study period (Fig. 4a).

During the study period, two major El Niño events (2009 and 2015) and three La Niña events (2008, 2011 and 2021) were identified (Fig. 4a and Methods). Overall, ocean NPP exhibits a much stronger response to El Niño–Southern Oscillation (ENSO) events than land NPP (Fig. 4b–e). On average, ocean NPP decreases by -0.97 ± 0.83 PgC yr^{-1} during El Niño events and increases by 0.70 ± 1.33 PgC yr^{-1} during La Niña events (Fig. 4b). By contrast, land NPP shows a decrease of -0.28 ± 0.13 PgC yr^{-1} during El Niño events and an increase of 0.12 ± 0.36 PgC yr^{-1} during La Niña events (Fig. 4c). ENSO-driven variability in ocean NPP primarily occurs in tropical oceans, particularly in the tropical Pacific and Indian oceans, while land NPP variability is concentrated in tropical and arid/semi-arid regions (Fig. 4d,e). These NPP anomalies are largely linked to ENSO-induced environmental anomalies, including drying/wetting on land and warming/cooling in the oceans (Extended Data Fig. 10 and Supplementary Fig. 4).

Discussion

We observe contrasting annual NPP trends over land and ocean from 2003 to 2021 (Figs. 1 and 2), primarily reflecting their divergent responses to climate warming (Fig. 3). On land, warming is associated with increased NPP, particularly in the boreal, alpine and parts of temperate zones (Fig. 3a–c), probably due to eased temperature limitations and extended growing seasons[5,11,33]. By contrast, ocean NPP declines, particularly in tropical waters (Fig. 3d–f), probably due to rising SST, which enhances stratification[34,35] and restricts the vertical nutrient transport essential[16,36,37] for phytoplankton growth, along with potential photoinhibition in the warmer, shallower mixed layer[38]. On land, additional drivers of enhanced NPP include regional wetting trends and non-climatic factors such as CO_2 fertilization, nitrogen deposition, reforestation and agricultural intensification, as reflected by increases in LAI[11,39]. However, in tropical America, NPP declines are probably linked to warming-induced water stress and drought conditions[9,40] (Extended Data Fig. 6), as well as disturbances such as deforestation[12,15] and wildfires[11,41]. In the ocean, enhanced NPP in mid and high latitudes are associated with increased surface PAR, ocean warming (Fig. 3d,e) and sea ice retreat[42–44], which help alleviate light and/or thermal limitations on phytoplankton growth[38].

Fig. 3 | Putative environmental controls on annual NPP trends over land and ocean. a, Spatial patterns of major putative environmental controls on land NPP trends, including annual surface PAR, TA and PRE. **b**, Annual trends of major land environmental factors shown as Theil–Sen slopes. **c**, Zonal statistics of key impacts factors associated with land NPP change. **d**, Spatial patterns of major putative environmental controls of ocean NPP trends, including annual sea surface PAR, SST and MLD. In **a** and **d**, the symbols '+' and '−' represent changes in environmental factors associated with increasing and decreasing NPP trends, respectively. The areas with statistically nonsignificant NPP trends ($P > 0.05$) are masked. **e**, Annual trends of major ocean environmental factors shown as Theil–Sen slopes. **f**, Zonal statistics of key impacts factors associated with ocean NPP change. Zone classifications are shown in Extended Data Fig. 5. In **c** and **f**, the relative area represents the fraction of each association type (positive or negative) relative to the total area of significant NPP change within each zone, as shown in **a** and **d**. The bold values highlight the dominant factor in each zone. **g**, Structural equation modeling (SEM) of direct environmental effects (light blue background) on land NPP without (left) and with (right) the latent variable of LAI; purple background. **h**, SEM of direct environmental effects on ocean NPP without (left) and with (right) the latent variables of MPAR and CHL (both purple background). In **g** and **h**, the arrow thickness indicates the strength of standardized path coefficients, representing the change in the target variable per s.d. change in the predictor. Green arrows denote positive effects and red arrows denote negative effects. Asterisks indicate statistical significance: $^*P \leq 0.05$ and $^{**}P \leq 0.01$. Zonal SEM results for land and ocean NPP are shown in Extended Data Figs. 7 and 8.

Overall, global NPP exhibits a strong upwards trend, primarily driven by increases in land NPP (Fig. 1), highlighting the critical role of terrestrial productivity in compensating for marine NPP losses at the biosphere level[8].

While land NPP dominates the long-term global trend (Fig. 1), we find that ocean NPP primarily regulates the interannual variability in global NPP (Fig. 4). This dominance probably stems from the rapid life cycle of phytoplankton, strong and dynamic ocean–atmosphere coupling and the physically open structure of marine environments, which facilitates the rapid and widespread propagation of climate signals, thereby amplifying their impacts on phytoplankton[4,8,17]. Notably, ocean NPP exhibits heightened sensitivity to ENSO-related climate anomalies compared with land (Fig. 4), consistent with patterns observed during an early ENSO transition from 1997 to 2000 (refs. 7,10). We observe a shift in ocean NPP from decreasing to increasing around 2015 (Fig. 4), primarily driven by reduced tropical NPP

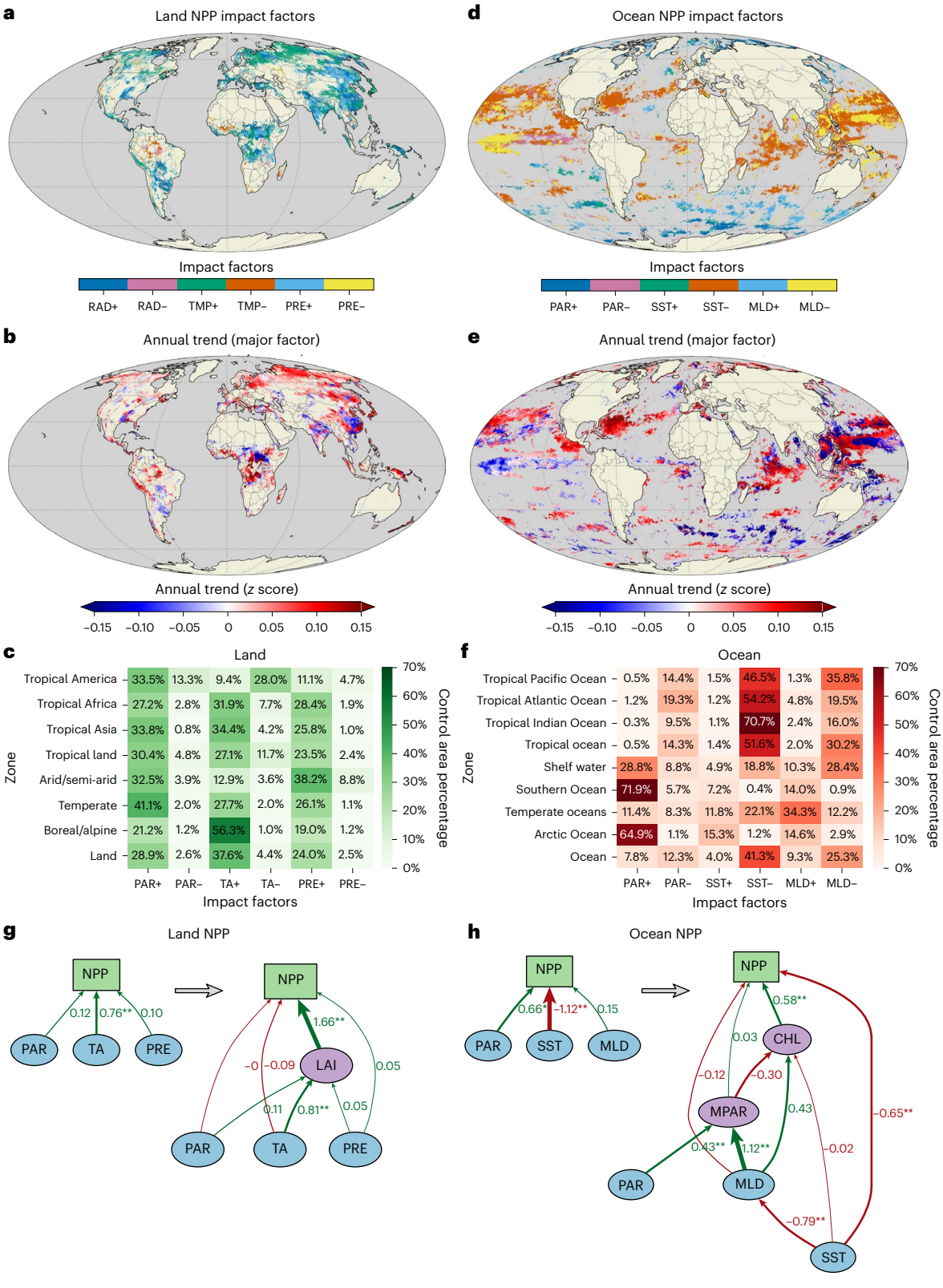

https://doi.org/10.1038/s41558-025-02375-1

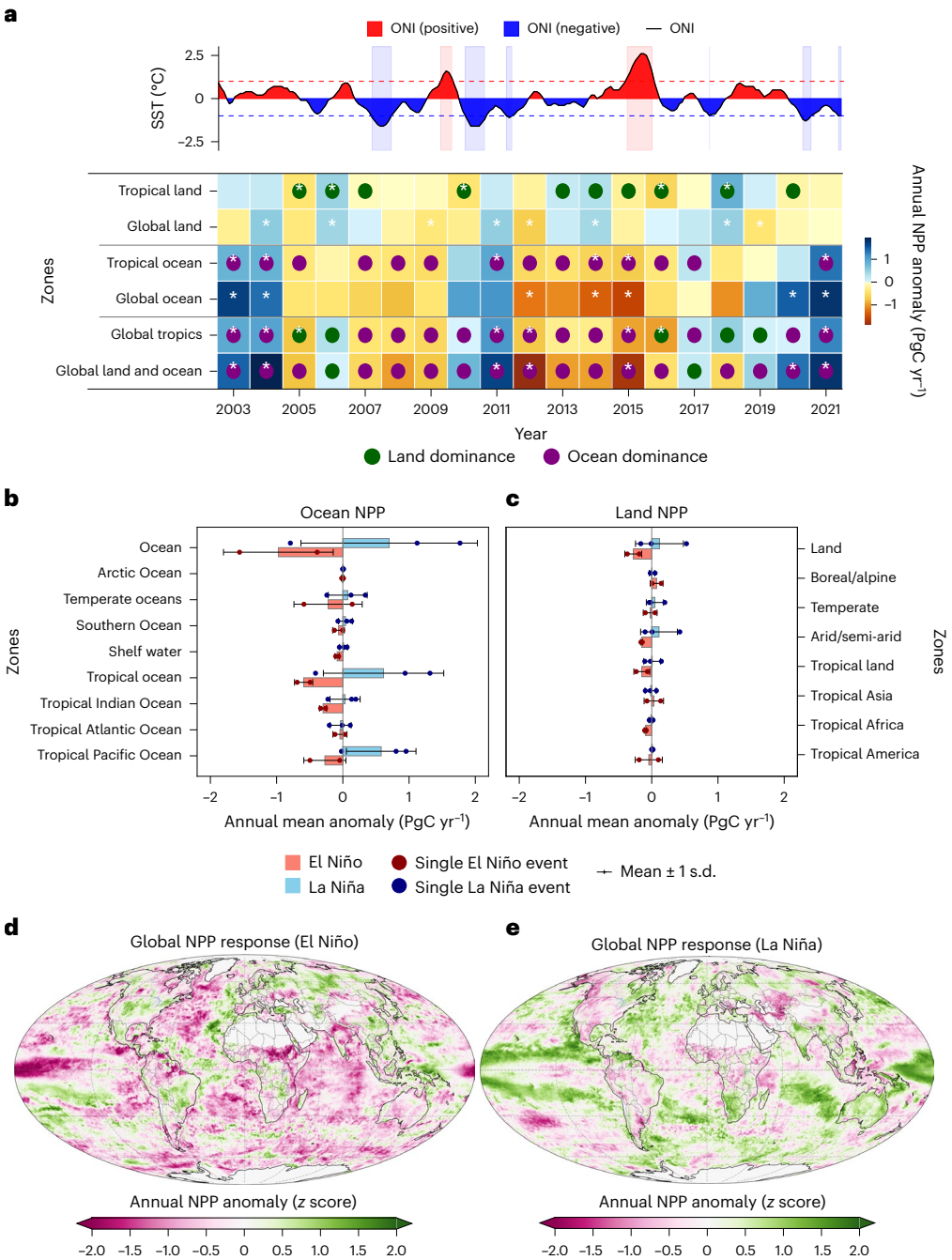

Fig. 4 | El Niño–Southern Oscillation (ENSO)-driven interannual variability in land and ocean NPP from 2003 to 2021. a, Annual anomalies in land, ocean and global NPP in relation to ENSO evolution. Area-weighted annual NPP values are detrended and anomalies are calculated relative to the multiyear mean (2003–2021). The zone with the highest absolute anomaly each year is marked with solid green circles for land NPP ('land dominance') and solid purple circles for ocean NPP ('ocean dominance'). Zonal NPP values with *z* scores (defined as the ratio of the annual anomaly to the multiyear s.d.) greater than 1 are labelled with a white asterisk. Moderate to strong ENSO events, identified by ONI >1 °C, are shaded in red (El Niño) and blue (La Niña). **b**, Average ocean NPP responses to ENSO events across different zones. **c**, Average land NPP responses to ENSO events across different zones. The error bars in **b** and **c** represent 1 s.d. during identified ENSO events (two for El Niño and three for La Niña; Methods). Zone classifications are shown in Extended Data Fig. 5. **d**, Mean global NPP responses during the identified El Niño years. **e**, Mean global NPP responses during the identified La Niña years. All values are standardized as *z* scores, calculated by dividing annual anomalies by the multiyear s.d. (2003–2021).

losses probably linked to a series of La Niña events beginning in late 2016 and peaking in 2021 (Extended Data Figs. 2 and 9), and enhanced mid- and high-latitude NPP, probably due to eased light and thermal constraints (Supplementary Fig. 2). However, this recent reversal has not reversed the overall declining trend observed from 2003 to 2021 (Fig. 1b). Whether this uptick represents a transient fluctuation or the onset of a sustained recovery remains uncertain and warrants continued monitoring. Given the projections of increasingly frequent and extreme ENSO events, particularly El Niño[45,46], the heightened sensitivity of oceanic NPP underscores a greater vulnerability of marine ecosystems to future climate variability[47], potentially leading to more pronounced fluctuations in the oceanic biological carbon pump[27] and thus global carbon sink[4]. Furthermore, the generally synchronized responses of land and ocean NPP to ENSO (Fig. 4) suggest a mechanism

through which future climate extremes could further amplify the variability in global biological carbon uptake.

We identify a latitudinally symmetric distribution of global NPP, marked by a primary peak in the tropics supported by both land and ocean productivity, and secondary peaks at the northern mid-latitudes (land dominated) and southern mid-latitudes (ocean dominated) (Fig. 2). Despite notable differences in land and ocean surface area and photosynthetic capacity, this balanced NPP distribution reflects a key biological productivity pattern for the biosphere[2], fundamentally regulating local food webs, biodiversity and biogeochemical cycles across hemispheric latitudinal gradients[8]. However, the tropical NPP peak exhibits a declining trend in the ocean and only a modest increase on land (Fig. 2), potentially weakening the foundation of tropical food webs and triggering cascading effects on biodiversity, fisheries and local economies[15,48]. Over time, these disruptions may increase the likelihood of the tropical oceans becoming a stronger net carbon source[4], while diminishing the capacity of tropical lands to function as effective carbon sinks[5]—thereby amplifying the impacts of climate warming. Notably, the observed increases in both land and ocean NPP at mid- and high-latitude regions, coupled with stagnation and decline in the tropics, may further signal a potential redistribution of the global carbon sink towards higher latitudes [4,9,15,49], though this pattern may also be shaped by the distinct physical mechanisms governing carbon uptake in terrestrial and marine systems[4,50]. However, we recognize that current RS-based NPP products remain limited by uncertainties in both algorithms and model inputs[19,20,23], and may not fully capture the complexity of NPP dynamics and their underlying drivers, particularly those associated with vertical processes in marine environments and fine-scale terrestrial responses, such as root-zone water availability and nitrogen limitation[8,11,17]. Continued research—supported by expanded in situ observations (such as flux networks on land and Argo profiling floats in the ocean), the strategic integration of targeted models and experiments, and the synergistic use of both traditional and emerging satellite missions with finer spatial, temporal and spectral resolutions (such as NASA's NISAR and PACE)—will be crucial for validating and further refining the conclusions of this study.

In summary, our findings demonstrate a net increase in the global NPP since the early 2000s, with contrasting contributions from land and ocean. The heightened temperature sensitivity of NPP, especially in tropical oceans, suggests a potential risk of reduced productivity under continued climate warming and more frequent extreme El Niño events. Projections using emergent constraints indicate a decline in tropical ocean NPP due to sustained warming[51], with implications for a continued downturn in global marine productivity by the end of this century[36]. Conversely, terrestrial greening is expected to persist across a range of climatic scenarios[11,52]. However, the magnitude of land-based NPP gains may be moderated by intensifying drought[53], nitrogen limitation[54] and anthropogenic disturbances[55]. Whether the declining trend in ocean productivity will continue and the extent and duration to which sustained increases in terrestrial productivity can compensate for oceanic losses remain critical open questions with far-reaching consequences for global carbon cycling and planetary health[4,8,49]. Addressing these questions will require sustained, coordinated monitoring of both land and ocean ecosystems as coupled components of the Earth system[1,8]. Such efforts are essential for advancing our understanding of the biosphere's resilience and vulnerability as both a key regulator of planetary boundaries[56,57] and a vital natural climate solution on a warming planet[58,59].

Online content

Any methods, additional references, Nature Portfolio reporting summaries, source data, extended data, supplementary information, acknowledgements, peer review information; details of author contributions and competing interests; and statements of data and code availability are available at https://doi.org/10.1038/s41558-025-02375-1.

References

1. Steffen, W. et al. The emergence and evolution of Earth System Science. *Nat. Rev. Earth Environ.* **1**, 54–63 (2020).
2. Field, C. B., Behrenfeld, M. J., Randerson, J. T. & Falkowski, P. Primary production of the biosphere: integrating terrestrial and oceanic components. *Science* **281**, 237–240 (1998).
3. O'Neill, D. W., Fanning, A. L., Lamb, W. F. & Steinberger, J. K. A good life for all within planetary boundaries. *Nat. Sustain.* **1**, 88–95 (2018).
4. Gruber, N. et al. Trends and variability in the ocean carbon sink. *Nat. Rev. Earth Environ.* **4**, 119–134 (2023).
5. Ruehr, S. et al. Evidence and attribution of the enhanced land carbon sink. *Nat. Rev. Earth Environ.* **4**, 518–534 (2023).
6. Zeng, Z. et al. Climate mitigation from vegetation biophysical feedbacks during the past three decades. *Nat. Clim. Change* **7**, 432–436 (2017).
7. Behrenfeld, M. J. et al. Biospheric primary production during an ENSO transition. *Science* **291**, 2594–2597 (2001).
8. Crisp, D. et al. How well do we understand the land–ocean–atmosphere carbon cycle? *Rev. Geophys.* **60**, e2021RG000736 (2022).
9. Zhao, M. & Running, S. W. Drought-induced reduction in global terrestrial net primary production from 2000 through 2009. *Science* **329**, 940–943 (2010).
10. O'Sullivan, M. et al. Climate-driven variability and trends in plant productivity over recent decades based on three global products. *Glob. Biogeochem. Cycles* **34**, e2020GB006613 (2020).
11. Piao, S. et al. Characteristics, drivers and feedbacks of global greening. *Nat. Rev. Earth Environ.* **1**, 14–27 (2020).
12. Zhang, Y. et al. Earth's record-high greenness and its attributions in 2020. *Remote Sens. Environ.* **316**, 114494 (2025).
13. Novick, K. A. et al. The impacts of rising vapour pressure deficit in natural and managed ecosystems. *Plant Cell Environ.* **47**, 3561–3589 (2024).
14. Li, F. et al. Global water use efficiency saturation due to increased vapor pressure deficit. *Science* **381**, 672–677 (2023).
15. Zhang, Y., Song, C., Band, L. E. & Sun, G. No proportional increase of terrestrial gross carbon sequestration from the greening earth. *JGR Biogeosci.* **124**, 2540–2553 (2019).
16. Behrenfeld, M. J. et al. Climate-driven trends in contemporary ocean productivity. *Nature* **444**, 752–755 (2006).
17. Westberry, T. K., Silsbe, G. M. & Behrenfeld, M. J. Gross and net primary production in the global ocean: an ocean color remote sensing perspective. *Earth Sci. Rev.* **237**, 104322 (2023).
18. Gregg, W. W. & Rousseaux, C. S. Global ocean primary production trends in the modern ocean color satellite record (1998–2015). *Environ. Res. Lett.* **14**, 124011 (2019).
19. Ryan-Keogh, T. J., Tagliabue, A. & Thomalla, S. J. Global decline in net primary production underestimated by climate models. *Commun. Earth Environ.* **6**, 75 (2025).
20. Ryan-Keogh, T. J., Thomalla, S. J., Chang, N. & Moalusi, T. A new global oceanic multi-model net primary productivity data product. *Earth Syst. Sci. Data* **15**, 4829–4848 (2023).
21. Chen, J. M. et al. Vegetation structural change since 1981 significantly enhanced the terrestrial carbon sink. *Nat. Commun.* **10**, 4259 (2019).
22. Yu, T. et al. Estimation of global vegetation productivity from global land surface satellite data. *Remote Sens.* **10**, 327 (2018).
23. Endsley, K. A., Zhao, M., Kimball, J. S. & Devadiga, S. Continuity of global MODIS terrestrial primary productivity estimates in the VIIRS era using model-data fusion. *J. Geophys. Res. Biogeosci.* **128**, e2023JG007457 (2023).
24. Ito, A. A historical meta-analysis of global terrestrial net primary productivity: are estimates converging? *Glob. Change Biol.* **17**, 3161–3175 (2011).

25. Westberry, T., Behrenfeld, M. J., Siegel, D. A. & Boss, E. Carbon-based primary productivity modeling with vertically resolved photoacclimation. *Glob. Biogeochem. Cycles* **22**, 1–18 (2008).
26. Silsbe, G. M., Behrenfeld, M. J., Halsey, K. H., Milligan, A. J. & Westberry, T. K. The CAFE model: a net production model for global ocean phytoplankton. *Glob. Biogeochem. Cycles* **30**, 1756–1777 (2016).
27. Brewin, R. J. et al. Sensing the ocean biological carbon pump from space: a review of capabilities, concepts, research gaps and future developments. *Earth Sci. Rev.* **217**, 103604 (2021).
28. Seiler, C. et al. Are terrestrial biosphere models fit for simulating the global land carbon sink? *J. Adv. Model. Earth Syst.* **14**, e2021MS002946 (2022).
29. Friedlingstein, P. et al. Global carbon budget 2023. *Earth Syst. Sci. Data* **15**, 5301–5369 (2023).
30. Román, M. O. et al. Continuity between NASA MODIS collection 6.1 and VIIRS collection 2 land products. *Remote Sens. Environ.* **302**, 113963 (2024).
31. McClain, C. R., Franz, B. A. & Werdell, P. J. Genesis and evolution of NASA's satellite ocean color program. *Front. Remote Sens.* **3**, 938006 (2022).
32. Terhaar, J. et al. Assessment of global ocean biogeochemistry models for ocean carbon sink estimates in RECCAP2 and recommendations for future studies. *J. Adv. Model. Earth Syst.* **16**, e2023MS003840 (2024).
33. Keenan, T. F. & Riley, W. J. Greening of the land surface in the world's cold regions consistent with recent warming. *Nat. Clim. Change* **8**, 825–828 (2018).
34. Li, G. et al. Increasing ocean stratification over the past half-century. *Nat. Clim. Change* **10**, 1116–1123 (2020).
35. Sallée, J.-B. et al. Summertime increases in upper-ocean stratification and mixed-layer depth. *Nature* **591**, 592–598 (2021).
36. Moore, J. K. et al. Sustained climate warming drives declining marine biological productivity. *Science* **359**, 1139–1143 (2018).
37. D'Alelio, D. et al. Machine learning identifies a strong association between warming and reduced primary productivity in an oligotrophic ocean gyre. *Sci. Rep.* **10**, 3287 (2020).
38. Li, Z. et al. Ocean-scale patterns of environment and climate changes driving global marine phytoplankton biomass dynamics. *Sci. Adv.* **10**, eadm7556 (2024).
39. Zhu, Z. et al. Greening of the Earth and its drivers. *Nat. Clim. Change* **6**, 791–795 (2016).
40. Chen, S. et al. Amazon forest biogeography predicts resilience and vulnerability to drought. *Nature* **631**, 111–117 (2024).
41. Zhang, Y. et al. Global fire modelling and control attributions based on the ensemble machine learning and satellite observations. *Sci. Remote Sens.* **7**, 100088 (2023).
42. Thomalla, S. J., Nicholson, S.-A., Ryan-Keogh, T. J. & Smith, M. E. Widespread changes in Southern Ocean phytoplankton blooms linked to climate drivers. *Nat. Clim. Change* **13**, 975–984 (2023).
43. Lewis, K. M., Van Dijken, G. L. & Arrigo, K. R. Changes in phytoplankton concentration now drive increased Arctic Ocean primary production. *Science* **369**, 198–202 (2020).
44. Xue, T. et al. Southern Ocean phytoplankton under climate change: a shifting balance of bottom-up and top-down control. *Biogeosciences* **21**, 2473–2491 (2024).
45. Thirumalai, K. et al. Future increase in extreme El Niño supported by past glacial changes. *Nature* **634**, 374–380 (2024).
46. Hu, K., Huang, G., Huang, P., Kosaka, Y. & Xie, S.-P. Intensification of El Niño-induced atmospheric anomalies under greenhouse warming. *Nat. Geosci.* **14**, 377–382 (2021).
47. Tittensor, D. P. et al. Next-generation ensemble projections reveal higher climate risks for marine ecosystems. *Nat. Clim. Change* **11**, 973–981 (2021).
48. Huston, M. A. & Wolverton, S. The global distribution of net primary production: resolving the paradox. *Ecol. Monogr.* **79**, 343–377 (2009).
49. Fernández-Martínez, M. et al. Diagnosing destabilization risk in global land carbon sinks. *Nature* **615**, 848–853 (2023).
50. Friedlingstein, P. et al. Global Carbon Budget 2021. *Earth Syst. Sci. Data* **14**, 1917–2005 (2022).
51. Kwiatkowski, L. et al. Emergent constraints on projections of declining primary production in the tropical oceans. *Nat. Clim. Change* **7**, 355–358 (2017).
52. Zhao, Q., Zhu, Z., Zeng, H., Zhao, W. & Myneni, R. B. Future greening of the Earth may not be as large as previously predicted. *Agric. Meteorol.* **292**, 108111 (2020).
53. Cao, D. et al. Projected increases in global terrestrial net primary productivity loss caused by drought under climate change. *Earth's Futur.* **10**, e2022EF002681 (2022).
54. Wieder, W. R., Cleveland, C. C., Smith, W. K. & Todd-Brown, K. Future productivity and carbon storage limited by terrestrial nutrient availability. *Nat. Geosci.* **8**, 441–444 (2015).
55. Hou, H. et al. Future land use/land cover change has nontrivial and potentially dominant impact on global gross primary productivity. *Earth's Futur.* **10**, e2021EF002628 (2022).
56. Running, S. W. A measurable planetary boundary for the biosphere. *Science* **337**, 1458–1459 (2012).
57. Richardson, K. et al. Earth beyond six of nine planetary boundaries. *Sci. Adv.* **9**, eadh2458 (2023).
58. Griscom, B. W. et al. Natural climate solutions. *Proc. Natl Acad. Sci. USA* **114**, 11645–11650 (2017).
59. Hoegh-Guldberg, O., Northrop, E. & Lubchenco, J. The ocean is key to achieving climate and societal goals. *Science* **365**, 1372–1374 (2019).

Methods

Global NPP products

To conduct the global NPP analysis, we employ six contemporary satellite-based products: three land NPP products—MOD17 (refs. 9,23), GLASS[22,60] and BEPS[21], and three ocean NPP products—EVGPM[61,62], CbPM[25] and CAFE[26] (Supplementary Table 1). Terrestrial products integrate satellite surface observations, climate data and ground flux and inventory data to estimate NPP through modelled photosynthesis and AR. Oceanic products use satellite ocean surface reflectance data, CHL and phytoplankton physiology to model marine primary production. These products, developed using distinct algorithms and modelling frameworks, were selected for their global coverage, temporal consistency and established validation. Importantly, all products use Moderate Resolution Imaging Spectroradiometer (MODIS)-derived variables as key inputs (mentioned below) and are constrained by in situ observations, enabling a consistent, single sensor-based integration of terrestrial and marine productivity for global analysis.

Among land models, MOD17 estimates GPP using light-use efficiency theory, combining absorbed PAR with environmental constraints from low temperature and water stress, and then calculates the NPP by subtracting respiration losses based on biome- and temperature-specific functions[9,23]. GLASS adopts a revised light-use efficiency model to further consider the effects of CO_2 fertilization and radiation components on GPP and then converts GPP to NPP using carbon use efficiency derived from land-surface models from TRENDY[22,60]. BEPS, a process-based model, uses the Farquhar photosynthesis theory at the leaf level[21], integrates radiation transfer within the canopy and environmental drivers to estimate GPP, and then subtracts maintenance and growth respiration to obtain NPP. All three models rely on MODIS-derived inputs, such as LAI, fraction of absorbed PAR and land cover, together with climate and geophysical data to produce global NPP datasets since 2000.

Among ocean models, EVGPM estimates NPP using CHL, adjusting photosynthetic rates for SST and light availability throughout the euphotic zone[61,62]. Unlike the standard VGPM, EVGPM incorporates photoacclimation effects at high temperatures. By contrast, CbPM focuses on phytoplankton carbon biomass and growth rates, using optical measurements to estimate NPP[25]. The CAFE model takes a mechanistic approach, calculating NPP based on spectral light absorption, conversion efficiency and detailed water column optics[26]. Overall, EVGPM is straightforward and empirically grounded, leveraging widely available chlorophyll data. CbPM accounts for physiological variability and directly estimates biomass and growth rates to improve accuracy, while CAFE offers a detailed mechanistic approach, incorporating spectral and temporal light variations.

Three land products are available from 2001 to 2021, each with varying spatial and temporal resolutions: MOD17 (annual, ~5 × 5 km), GLASS (8 day, 0.5 × 0.5 km) and BEPS (daily, ~8 × 8 km). Three ocean products are from 2003–2023, all sharing the same spatial and temporal resolutions (monthly, ~10 × 10 km). To conduct interannual analysis, we aggregate all data to annual values for the overlapping period of 2003–2021, which avoids the potential influence of satellite orbit drift on MODIS products after 2021 (ref. 63). Ocean NPP products are based on the MODIS Reprocessing R2022 data, which features updated instrument calibration and algorithm improvements[64]. To retain spatial details, land analyses are conducted at 5 km and ocean analyses at 10 km resolution. We calculate ensemble means and standard deviations across the three land and three ocean products, resulting in nine land–ocean combinations for global NPP estimates (Extended Data Fig. 1). This ensemble approach integrates complementary model strengths, reduces potential individual product biases and yields a more robust estimate of global NPP.

Land and ocean classification zones

For global analysis, we apply a 5 × 5 km land mask based on the MODIS land cover product (MCD12C1 C61)[65], excluding non-vegetated areas (urban, barren, permanent snow and ice and water) using the dominant classification from 2003 to 2021. The 10 × 10 km ocean mask excludes perennial sea ice (areas with the multiyear mean NPP < 0.01 gC m^{-2} yr^{-1}) and omits freshwater lakes due to high uncertainty in ocean NPP estimates. For regional land analysis, we use the original 1 × 1 km Köppen–Geiger climate classification[66] to define four climate zones: tropical, arid/semi-arid, temperate and boreal/alpine, with the tropics further divided by continent (Extended Data Fig. 5a). Ocean regions are divided into six zones, including Pacific, Atlantic, Indian, Southern and Arctic oceans and shelf water from the marine and pelagic ecoregions of the World[67]. Three key oceans (Pacific, Atlantic and Indian) are further subdivided into tropical oceans (35° N to 35° S, encompassing the subtropical regions), northern temperate oceans (north of 35° N; not applicable to the Indian Ocean) and southern temperate oceans (south of 35° S). Note that the temperate ocean category also covers parts of the subpolar regions, up to 60° N in the north and 60° S in the south. Overall, these classification schemes enable detailed regional analyses while maintaining a global view of NPP dynamics across diverse land and ocean climate zones.

Global NPP trend and variability analysis

We assess annual trends in land, ocean and global NPP from 2003 to 2021 using Theil–Sen regression, a robust, nonparametric method that estimates the median slope of all pairwise comparisons by reducing sensitivity to outliers and non-normality[68]. Trend significance is tested with the Mann–Kendall test, with P values of 0.01–0.05 considered significant and those below 0.01 deemed extremely significant. For comparison, we also calculate linear trends using ordinary least squares regression (Fig. 1d). To examine the potential shifts or change points in the annual NPP trend, we conducte segmented linear regression analysis[69] for land, ocean and global datasets using the Python package pwlf (piecewise linear fit)[70]. Given the relatively short time series (2003–2021), we limit the analysis to a single change point in the annual NPP series to capture the most significant trend shift while minimizing the risk of overfitting. If a statistically significant change point was identified, annual NPP trends and their significance would be evaluated before and after the change point using Theil–Sen regression and the Mann–Kendall test (Fig. 1a–c).

To characterize the spatial variability of NPP across the globe, we use two complementary approaches. First, we conduct a latitudinal gradient analysis at 0.5° intervals for both land and ocean. For each latitudinal band, we calculate the area-weighted multiyear mean and long-term trend (2003–2021) in land, ocean and global NPP. This method enables a clear assessment of how terrestrial and marine ecosystems contribute to global NPP magnitude and trends from the equator to the poles (Fig. 2b,f). To determine whether land or ocean dominates NPP within each latitudinal band, we compare their absolute contributions to both mean values and trends. Second, we examine how NPP trends vary across different baseline productivity levels, using 17.5 and 5 gC m^{-2} yr^{-1} intervals for land (a total of 80 intervals from 0 to 1,400 gC m^{-2} yr^{-1}) and ocean (a total of 80 intervals from 0 to 400 gC m^{-2} yr^{-1}), respectively. Within each baseline interval, we compute both unit-area mean and area-weighted total NPP trends (Fig. 2g,h). This analysis would reveal the relationship between mean productivity levels and observed trends, allowing us to identify whether areas of high or low baseline NPP exhibit different patterns of change over time. Finally, land and ocean statistics on area-weighted total NPP, trends and interannual variability are calculated and compared across different climate zones (Extended Data Fig. 4 and Supplementary Fig. 3).

Putative attributions for land and ocean NPP trends

To examine the environmental drivers of annual NPP trends across land and ocean, we select key variables specific to each domain. For land, we assess the potential influence of PAR, TA and PRE, derived from the global ~4 km monthly TerraClimate dataset. For ocean, we

consider PAR, SST and MLD obtained from global ~10 km monthly MODIS-derived products. Sources of these global environmental datasets are provided in Supplementary Table 1. We perform Spearman's rank correlation analyses to examine the relationships between these environmental factors and NPP for each pixel. Rank correlations, which measure the strength and direction of associations between variables, help us identify which environmental factors most strongly influence NPP. By comparing these correlations (Supplementary Figs. 1 and 2), we determine the major impact factors for both land and ocean NPP pixel by pixel (Fig. 3a,d). Additionally, we calculate the trends of these influence factors to understand their temporal dynamics and how they might be driving changes in NPP (Fig. 3b,e).

To analyse the co-regulation of GPP and AR on annual NPP trends from 2003 to 2021, we apply Theil–Sen regression to classify pixel-level trends in GPP, AR and NPP as increasing or decreasing, and examine their co-occurrence patterns (Extended Data Fig. 6). This analysis is based on the MOD17 dataset, which estimates AR by accounting for its physiological coupling with GPP and temperature sensitivity of maintenance respiration based on the Q10 theory[23]. The dominant driver of NPP change is identified by comparing the absolute magnitudes of GPP and AR slopes at each pixel. We quantify the spatial extent of each trend combination and dominant driver type as a percentage of the global vegetated land area. Focusing on tropical regions, we further assess the potential effects of warming-induced water stress by analysing trends in PRE, TA and vapour pressure deficit and their influence on both GPP and AR. Spearman's rank correlation is used to evaluate the relationships among TA, vapour pressure deficit, GPP and NPP, enabling us to explore the compound effects of warming and water stress on tropical productivity and to assess the potential vulnerability of tropical ecosystems.

We further use SEM to elucidate the potential mechanisms behind the observed trends in land and ocean NPP. This statistical technique combines factor analysis and multiple regression to analyse complex relationships between variables[71], allowing us to quantify both direct and indirect effects of multiple environmental factors on NPP changes. Importantly, we note that SEM does not infer strict causality but rather identifies statistically supported relationships based on model structure and prior knowledge.

For land NPP, the SEM structure is designed to capture both direct and indirect effects. NPP is modelled as a function of PAR, TA, PRE and LAI. LAI, treated as a latent variable, is modelled as a function of the same environmental drivers (PAR, TA and PRE), reflecting its role as a mediator influenced by these factors. LAI serves as a latent variable potentially reflecting biomass change and capturing influences such as land use/cover change, CO_2 fertilization and nitrogen deposition[12,39], which are known to affect NPP but are not directly included in the model.

For ocean NPP, the SEM structure includes both direct and mediated pathways. NPP is modelled as a function of CHL, MPAR, SST and MLD. CHL is modelled as a function of MPAR, MLD and SST, while MPAR is modelled as a function of MLD and PAR. MLD itself is modelled as a function of SST. This hierarchical structure reflects hypothesized causal links whereby SST influences MLD, which in turn modulates MPAR and CHL, ultimately affecting NPP.

MPAR quantifies the light availability within the ocean's mixed layer, where most phytoplankton photosynthesis occurs. MPAR is calculated by integrating surface PAR over the MLD and accounting for vertical light attenuation[72]:

$$\mathrm{MPAR} = \int_0^{\mathrm{MLD}} \mathrm{PAR}_{\mathrm{Surface}} \times \mathrm{e}^{-kz}\mathrm{d}z = \mathrm{PAR}_{\mathrm{Surface}}\left(\frac{1-\mathrm{e}^{-k*\mathrm{MLD}}}{k}\right)$$

$$k = 0.0166 + 0.0733 \times \mathrm{CHL}^{0.6715}$$

where MPAR is MLD-integrated PAR (mol photons per m^2 per day), z is the depth below the sea surface (m), MLD is the mixed-layer depth (m), $\mathrm{PAR}_{\mathrm{surface}}$ is surface PAR (mol photons per m^2 per day), k is the light attenuation coefficient and CHL is the surface chlorophyll-a concentration (in milligrams per m^3). MPAR is calculated monthly and subsequently aggregated to annual values.

We construct SEMs for land and ocean NPP at both global (Fig. 3g,h) and regional scales (Extended Data Figs. 7,8) using maximum likelihood estimation implemented through the Python package semopy 2.3.11. Before SEM running, all input variables are standardized as z scores by subtracting the multiyear mean and dividing by the s.d. Direct and indirect effects are interpreted from the standardized path coefficients, which indicate the relative strength and direction of the associations between environmental drivers and NPP along hypothesized pathways. We emphasize that these results should be interpreted as statistical associations rather than definitive causal inferences.

We further acknowledge that the pathways proposed here are simplified representations of more complex processes. For example, MLD variability is influenced not only by changes in SST, but also by factors such as wind speed, salinity gradients and ocean circulation patterns[34]. CHL is influenced by additional factors beyond those considered here, such as species composition, nutrient uptake efficiency, light adaptation and grazing pressure[17]. Similarly, LAI is influenced by land-use change, forest management, nutrient deposition and disturbances such as fire and pests[11]. Our analysis reflects the necessary simplification of these inherently complex and interacting processes, aiming at capturing the dominant climatic associations with NPP at global and broad regional scales (Fig. 3g,h and Extended Data Figs. 7 and 8).

Evaluation of process-based NPP products

To evaluate process-based model performance in simulating global NPP, we analyse outputs from both land and ocean models in comparison with satellite-based estimates. On land, we use 16 DGVMs from the TRENDY v10 ensemble (2003–2020), a coordinated modelling effort supporting the Global Carbon Budget[50]. The models include CLASSIC, CLASSIC-N, VISIT, LPJ, IBIS, ISBA-CTRIP, YIBs, CABLE-POP, DLEM, ISAM, LPJ-GUESS, LPX-Bern, ORCHIDEE, SDGVM, CLM5.0 and ORCHIDEEv3. For the ocean, we select 15 GOBMs participating in CMIP6 historical simulations (2003–2014). These models include CESM2-WACCM, CNRM-ESM2-1, MPI-ESM1-2-HR, GFDL-ESM4, CanESM5, UKESM1-0-LL, NorESM2-LM, MRI-ESM2-0, CMCC-ESM2, CESM2, EC-Earth3-CC, ACCESS, NorESM2-MM, IPSL-CM6A-LR and MPI-ESM1-2-LR. Since 2015, CMIP6 model outputs are based on future scenario simulations; therefore, we limit our analysis to the historical period before 2015. For both DGVMs and GOBMs, the yearly aggregated NPP output are resampled to 1° spatial resolution for analysis. Comparisons between process-based (DGVMs and GOBMs) and RS-based NPP products are conducted using ensemble means and standard deviations to assess intermodel variability and trend consistency during their overlapping periods (Fig. 2g,h and Extended Data Fig. 3).

ENSO-driven interannual variability in land and ocean NPP

ENSO is a recurring climate phenomenon across the tropical Pacific Ocean, characterized by the warm phase of El Niño and cool phase of La Niña. We use the Oceanic Niño Index (ONI) from NOAA to classify El Niño and La Niña events, which can potentially influence extensive climate anomalies across both global oceans and land. In this study, we identify two El Niño events (2009–2010 and 2015–2016) and three La Niña events (2007–2008, 2010–2011 and 2020–2021), categorized as moderate or strong, each meeting the criterion of five consecutive overlapping 3 month periods with ONI at or above +1° for El Niño and at or below −1° for La Niña (Fig. 4a). To facilitate the annual analysis and avoid mixed ENSO signals, we further narrow down individual years dominated by El Niño (2009 and 2015) and La Niña (2008, 2011 and 2021) events for analysing responses in both land and ocean NPP and their environmental factors. We then calculate the average anomalies

and standard deviations for annual NPP (Fig. 4b–e) and relevant environmental factors (Extended Data Fig. 10 and Supplementary Fig. 4) during these identified ENSO years across different climate zones. To better reflect the interannual variability, we detrend all annual NPP and environmental factors. The dominance of tropical regions in annual land or ocean NPP anomalies, as well as the dominance of land or ocean in global NPP anomalies, are determined by comparing their absolute values (Fig. 4a).

Reporting summary

Further information on research design is available in the Nature Portfolio Reporting Summary linked to this article.

Data availability

All global satellite and geophysical products needed to evaluate the conclusions in this article are publicly available, with their respective access links provided in Supplementary Table 1. The generated global land and ocean means and their annual trends and significance from 2003 to 2021 are available via the Open Science Framework repository[73]. An interactive tool for the visualization of the key global NPP metrics including multiyear mean, annual trend, interannual variability and specific yearly anomaly is available online[74].

Code availability

All codes needed to reproduce the key findings in this article are available via the Open Science Framework repository[73].

References

60. Huang, X. et al. High spatial resolution vegetation gross primary production product: algorithm and validation. *Sci. Remote Sens.* **5**, 100049 (2022).
61. Behrenfeld, M. J. & Falkowski, P. G. Photosynthetic rates derived from satellite-based chlorophyll concentration. *Limnol. Oceanogr.* **42**, 1–20 (1997).
62. EPPLEY, R. W. Temperature and phytoplankton growth in the sea. *Fish. Bull.* **70**, 1063–1085 (1971).
63. Twedt, K., Xiong, X., Geng, X., Wilson, T. & Mu, Q. Impact of satellite orbit drift on MODIS Earth scene observations used in calibration of the reflective solar bands. In *Proc. Earth Observing Systems XXVIII* Vol. 12685, 158–167 (SPIE, 2023).
64. MODIS/Aqua ocean color reprocessing 2022.0. *NASA* https://oceancolor.gsfc.nasa.gov/data/reprocessing/r2022/aqua/ (2025).
65. Sulla-Menashe, D., Gray, J. M., Abercrombie, S. P. & Friedl, M. A. Hierarchical mapping of annual global land cover 2001 to present: the MODIS Collection 6 Land Cover product. *Remote Sens. Environ.* **222**, 183–194 (2019).
66. Beck, H. E. et al. Present and future Köppen–Geiger climate classification maps at 1-km resolution. *Sci. Data* **5**, 1–12 (2018).
67. *Marine Ecoregions and Pelagic Provinces of the World. GIS Layers Developed by The Nature Conservancy with Multiple Partners, Combined from Spalding et al. (2007) and Spalding et al. (2012)* (The Nature Conservancy, 2012).
68. Dang, X., Peng, H., Wang, X. & Zhang, H. Theil–Sen estimators in a multiple linear regression model. *Olemiss Edu.* **2**, 1–30 (2008).
69. Tomé, A. R. & Miranda, P. M. A. Piecewise linear fitting and trend changing points of climate parameters. *Geophys. Res. Lett.* **31**, 1–4 (2004).
70. pwlf: piecewise linear fitting https://jekel.me/piecewise_linear_fit_py (2025).
71. Bowen, N. K. & Guo, S. *Structural Equation Modeling* (ed. Brockveld, K. C.) Oxford Univ. Press, 2011).
72. Li, Z. & Cassar, N. A mechanistic model of an upper bound on oceanic carbon export as a function of mixed layer depth and temperature. *Biogeosciences* **14**, 5015–5027 (2017).
73. Zhang, Y. & Cassar, N. Data and Python codes for 'Contrasting biological production trends over land and ocean'. *Open Science Framework* https://doi.org/10.17605/OSF.IO/86K3N (2025).
74. Zhang, Y. Interactive tool for 'Planetary Photosynthetic Productivity'. *Google Earth Engine App* https://planetlab.users.earthengine.app/view/p3npp (2025).

Acknowledgements

We gratefully acknowledge the NASA MODIS Ocean and Land Science Teams, M. Behrenfeld (Oregon State University), M. Zhao (NASA Goddard Space Flight Center), K. A. Endsley (University of Montana), S. Liang (University of Maryland), W. Ju (Nanjing University) and J. Chen (University of Toronto) for providing global ocean and land NPP products. We also thank the modelling groups contributing to CMIP6 for their ocean biogeochemistry simulations and the TRENDY project teams for their terrestrial biosphere model outputs, as coordinated through the Global Carbon Budget initiative. In addition, we extend our sincere appreciation to the institutions and researchers listed in Supplementary Table 1 for making the publicly available land and ocean datasets used in this study. Y.Z., W.L. and G.S. are partially supported by the Duke University–USDA Forest Service collaboration (grant no. 23-JV-11330180-119). N.C. is supported by the National Science Foundation (grant no. OCE-2123198). J.X. is supported by the National Science Foundation (Macrosystem Biology and NEON-Enabled Science program: grant no. DEB-2017870). J.M. is supported by the Oak Ridge National Laboratory (ORNL) through the 'Reducing Uncertainties in Biogeochemical Interactions through Synthesis and Computing' scientific focus area and the 'Terrestrial Ecosystem Science Scientific' focus area, funded by the Earth and Environmental Systems Sciences Division of the Biological and Environmental Research Office within the US Department of Energy Office of Science. ORNL is managed by UT-Battelle, LLC, for the DOE under contract DE-AC05-00OR22725.

Author contributions

Y.Z. and N.C. conceived the idea and designed the research. Y.Z., N.C., W.L., G.S., M.D., J.M., Z.L. and Q.Z. developed the methodology. Y.Z. and N.C. carried out the investigation. Y.Z. performed the data visualization and wrote the original draft of the paper. All authors, including Y.Z., N.C., W.L., G.S., J.M., M.D., J.X., Z.L., H.Z., Q.Z., S.H. and C.S., discussed the design, methods and results, and contributed to the writing, review, and editing of the paper

Competing interests

The authors declare no competing interests.

Additional information

Extended data is available for this paper at https://doi.org/10.1038/s41558-025-02375-1.

Supplementary information The online version contains supplementary material available at https://doi.org/10.1038/s41558-025-02375-1.

Correspondence and requests for materials should be addressed to Yulong Zhang or Nicolas Cassar.

Peer review information *Nature Climate Change* thanks Steven Running, Rui Sun and Toby Westberry for their contributions to the peer review of this work.

https://doi.org/10.1038/s41558-025-02375-1

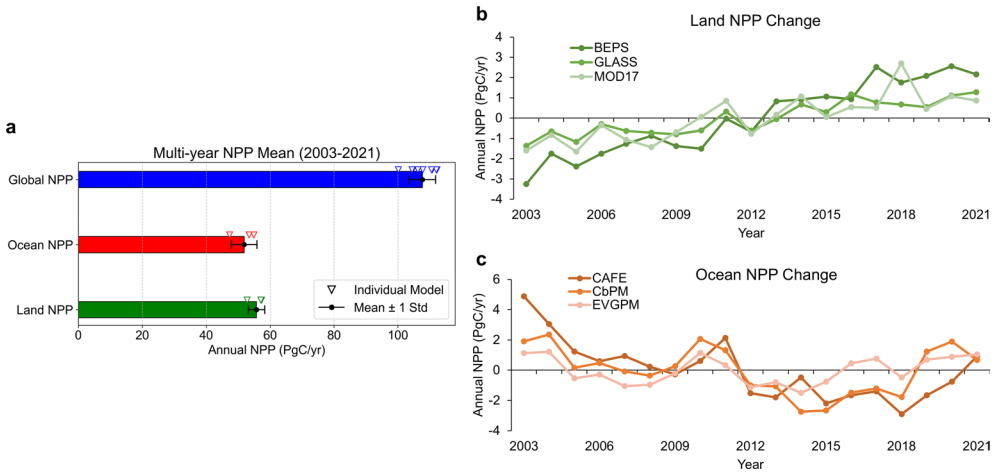

Extended Data Fig. 1 | Comparison of global ensemble means and interannual variability in land and ocean NPP based on remote sensing products from 2003 to 2021. a, Ensemble means of land NPP (N = 3), ocean NPP (N = 3) and global total NPP (N = 9). **b**, Annual land NPP changes from three RS-based products (BEPS, GLASS and MOD17). **c**, Annual ocean NPP changes from three RS-based products (CAFE, CbPM and EVGPM). In **a**, error bars represent the standard deviations across three models for both land and ocean NPP, as well as nine annual combinations for global NPP. Annual NPP anomalies in **b** and **c** are calculated relative to the multi-year mean (2003–2021) of each modeled NPP.

https://doi.org/10.1038/s41558-025-02375-1

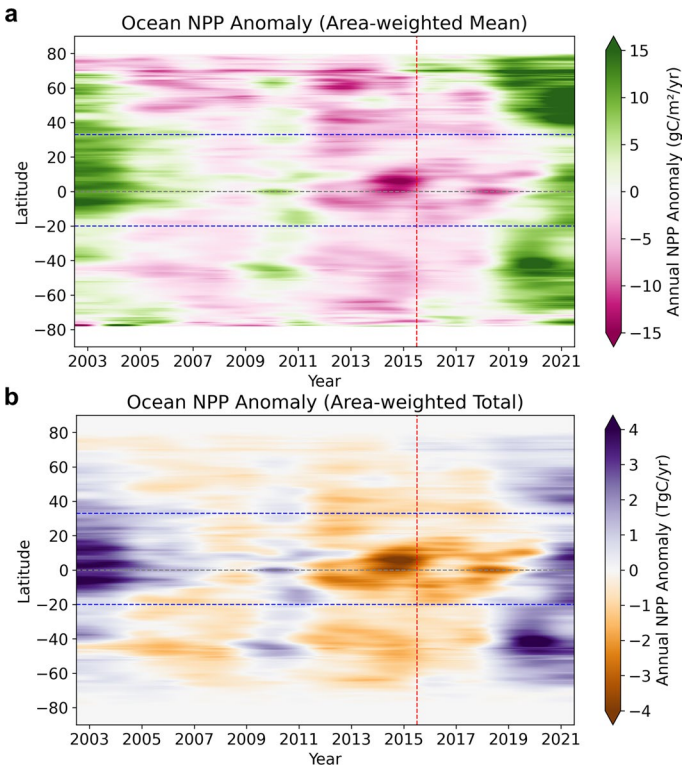

Extended Data Fig. 2 | Annual ocean NPP changes along the latitudinal gradient (1° interval) from 2003 to 2021. a, Annual NPP anomalies expressed as latitudinal area-weighted mean. **b**, Annual NPP anomalies expressed as latitudinal area-weighted total. In both panels, anomalies are calculated relative to the multiple year mean within each latitudinal band. The vertical line marks the 2015 breakpoint in the global ocean NPP trend, as shown in Fig. 1b. Two horizontal lines denote the mid- to high-latitude regions, where the decline-to-increase reversal in NPP is mainly observed.

https://doi.org/10.1038/s41558-025-02375-1

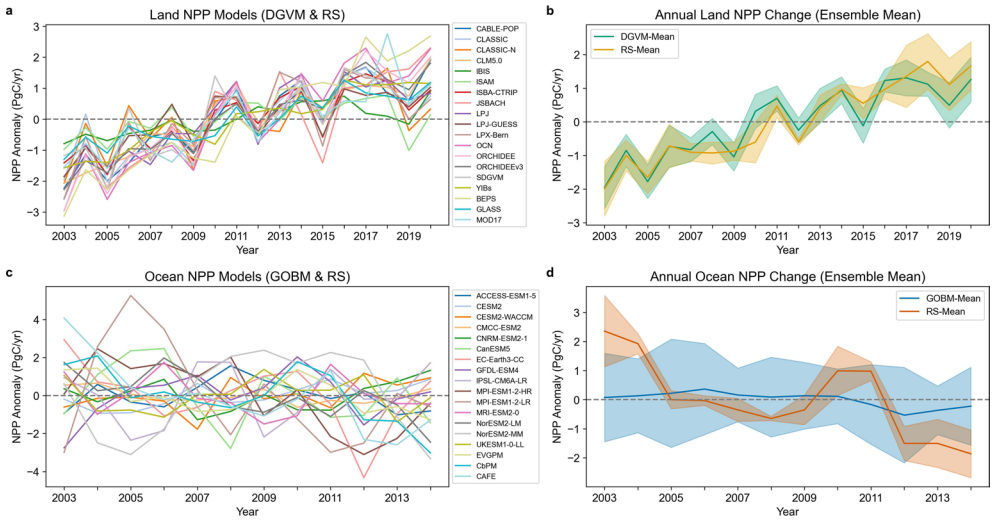

Extended Data Fig. 3 | Evaluation of processed-based models in simulating land and ocean NPP with remote sensing (RS)-based models. a, Annual land NPP from 16 Dynamic Global Vegetation Models (DGVMs) and three RS-based models. **b**, Annual land NPP from the ensemble means of DGVM (DGVM-Mean) and RS-based models (RS-Mean), with shaded areas representing one standard deviation among each model group. **c**, Annual ocean NPP from 15 Global Ocean Biogeochemistry Models (GOBMs) and three RS-based models. **d**, Annual ocean NPP from the ensemble means of GOBMs (GOBM-Mean) and RS-based models (RS-Mean), with shaded areas representing one standard deviation among each model group. In **a, b**, DGVMs are from TRENDY V10 (2003 to 2020); In **c, d**, GOBMs are from historic simulations from CMIP6 (2003 to 2014).

https://doi.org/10.1038/s41558-025-02375-1

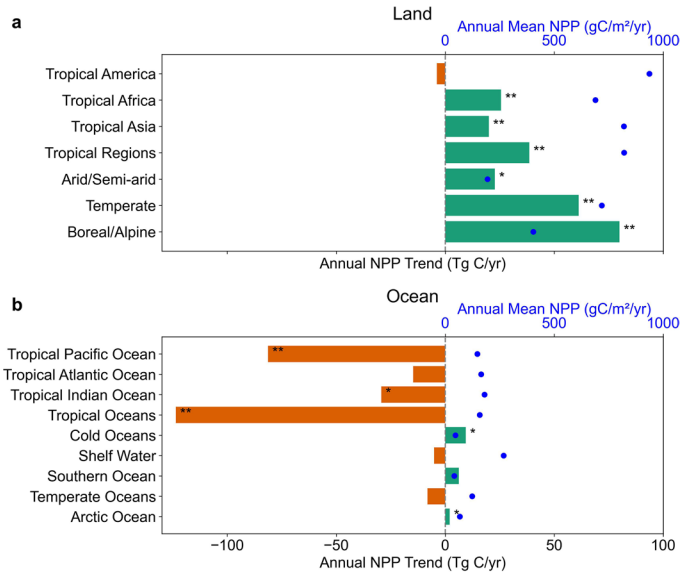

Extended Data Fig. 4 | Annual NPP trends and multi-year baseline NPP from 2003 to 2021 across land and ocean zones. a, Land zones; **b**, Ocean zones. Land and ocean zones are shown in Extended Data Fig. 5. In **b**, cold oceans includes Southern Ocean and Arctic Oceans. Trends are calculated using Theil–Sen regression, with two-sided statistical significance assessed by the Mann–Kendall test (*$P \le 0.05$; **$P \le 0.01$).

https://doi.org/10.1038/s41558-025-02375-1

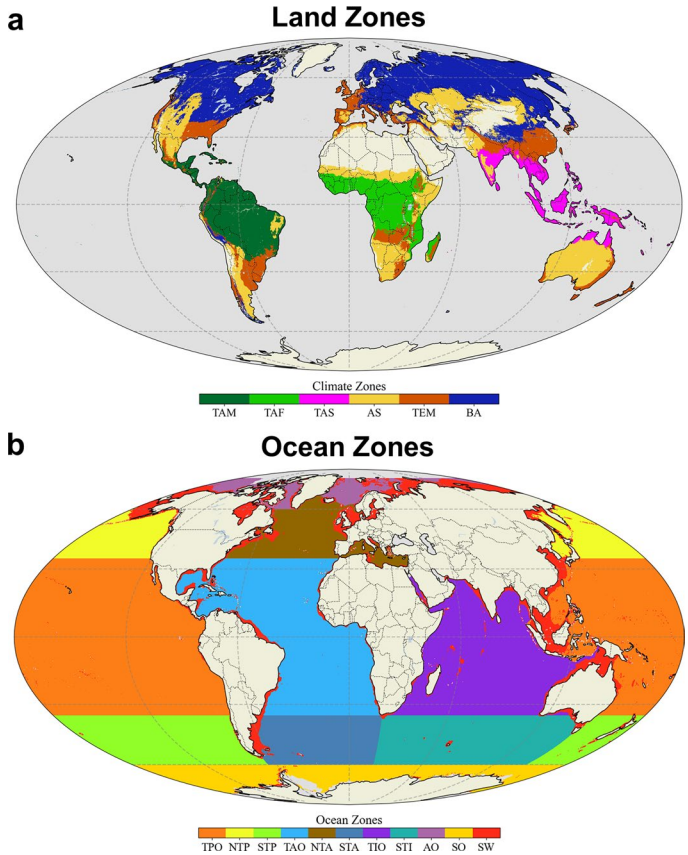

Extended Data Fig. 5 | Global zone classifications used in this study. a, Land zones. **b**, Ocean zones. In **a**, terrestrial zones include TAM (Tropical America), TAF (Tropical Africa), TAS (Tropical Asia), AS (Arid/Semi-arid), TEM (Temperate), and BA (Boreal/Alpine). In b, marine zones include TPO (Tropical Pacific Ocean), NTP (Northern Temperate Pacific Ocean), STP (Southern Temperate Pacific Ocean), TAO (Tropical Atlantic Ocean), NTA (Northern Temperate Atlantic Ocean), STA (Southern Temperate Atlantic Ocean), TIO (Tropical Indian Ocean), STI (Southern Temperate Indian Ocean), AO (Arctic Ocean), SO (Southern Ocean), and SW (Shelf Water).

https://doi.org/10.1038/s41558-025-02375-1

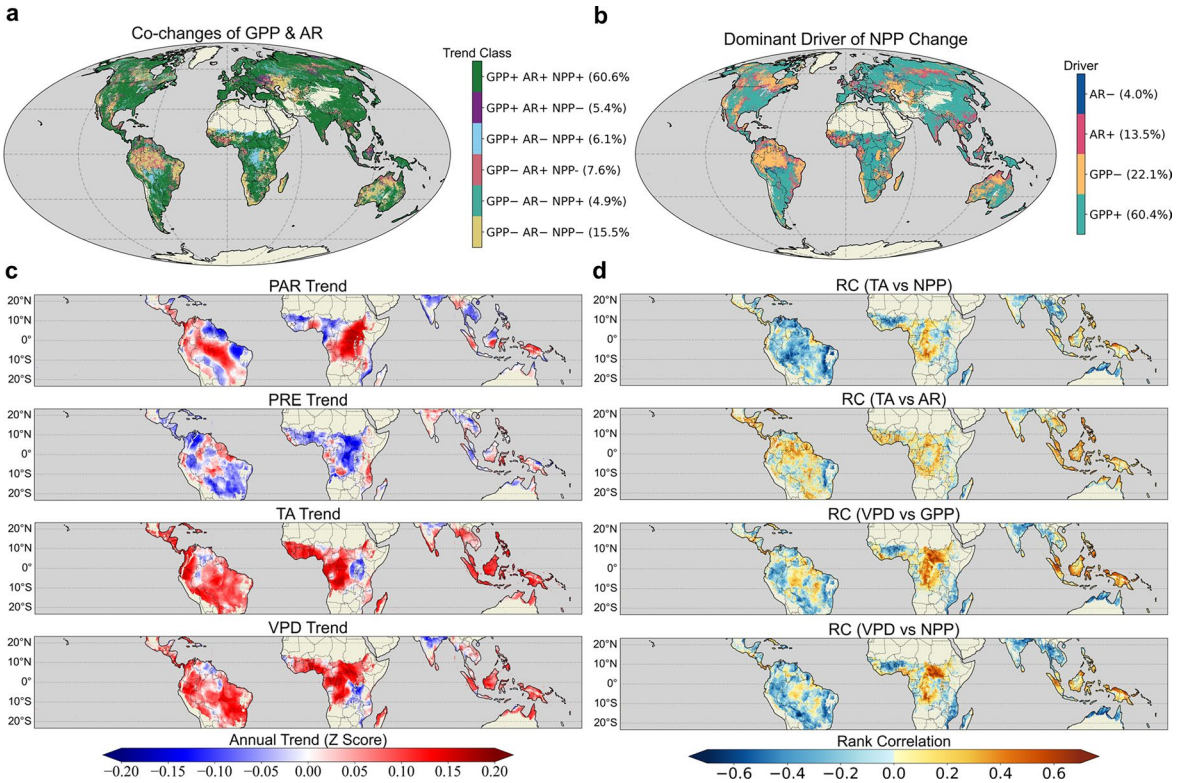

Extended Data Fig. 6 | Co-regulation of gross primary production (GPP) and autotrophic respiration (AR) on annual NPP changes from 2003 to 2021. **a**, Co-occurring trends of GPP and AR and their associations with NPP trends. Change classes are based on annual Theil-Sen's slope: + (slope > 0), − (slope < 0). For example, GPP + AR + NPP+ indicates that positive trends in both GPP and AR are associated with an increase in NPP. **b**, Dominant drivers of NPP trends based on the relative magnitude of GPP and AR slopes. For instance, AR+ indicates that the absolute Theil-Sen's slope of AR exceeds that of GPP, suggesting AR as the dominant influence on NPP. In **a** and **b**, values in parentheses represent the percentage of area relative to the global total vegetated land surface. **c**, Annual trends of key climate variables over tropical regions, including photosynthetically active radiation (PAR), precipitation, air temperature (TA), and vapor pressure deficit (VPD). **d**, Rank correlations among TA, VPD, GPP, and NPP across the tropical region.

https://doi.org/10.1038/s41558-025-02375-1

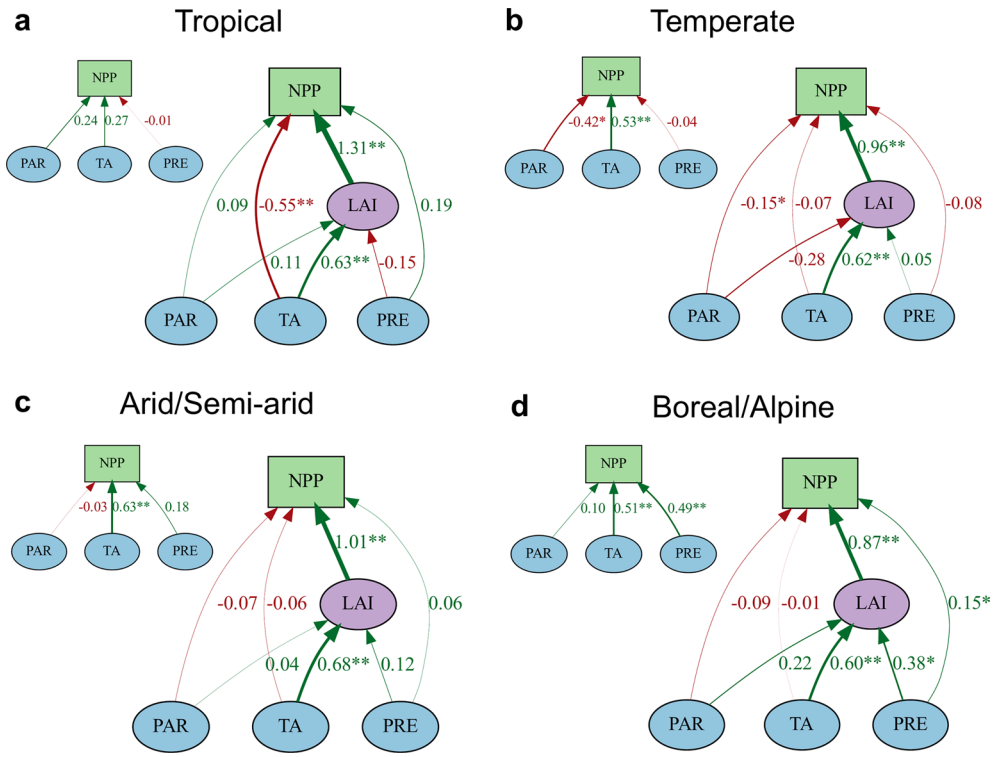

Extended Data Fig. 7 | Structural equation modeling of environmental effects on land NPP trends across different zones. a-d: tropical, temperate, arid/semi-arid and boreal/alpine zones (shown in Extended Data Fig. 5). Climatic variables and path coefficient descriptions are consistent with those presented in Fig. 3g.

https://doi.org/10.1038/s41558-025-02375-1

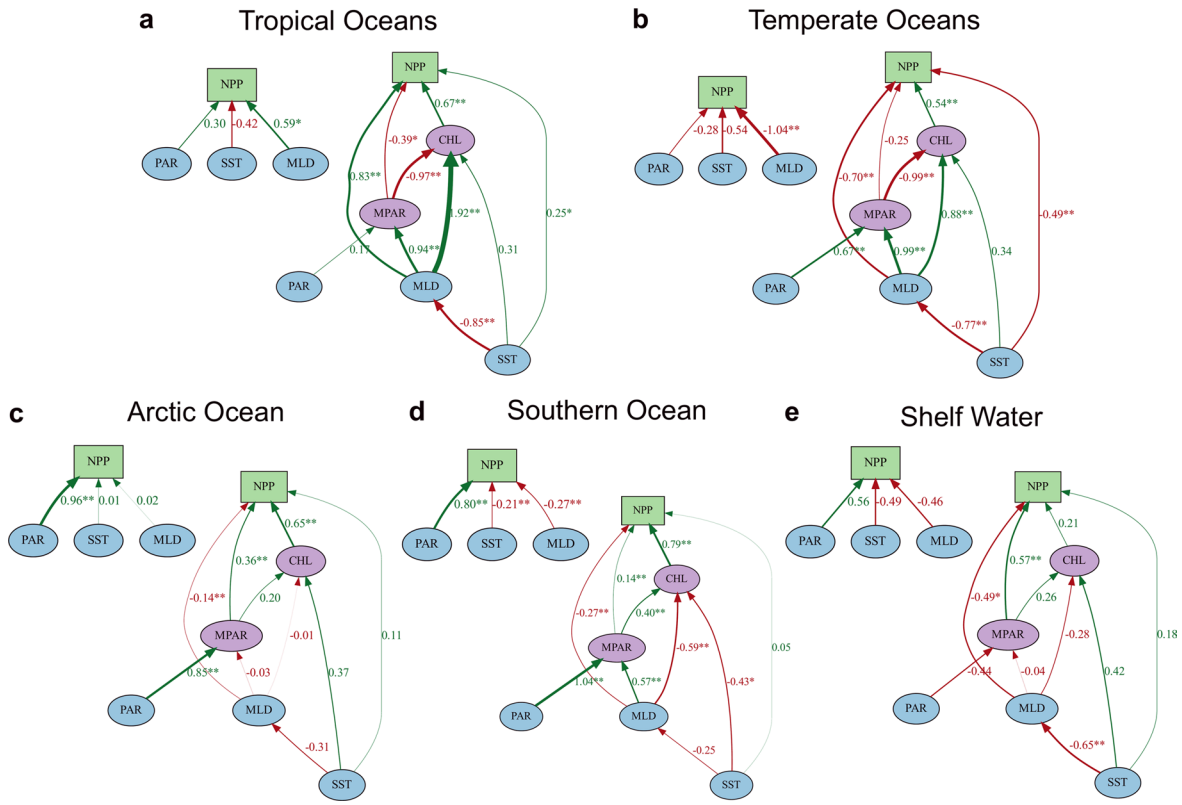

Extended Data Fig. 8 | Structural equation modeling of environmental effects on ocean NPP trends across different zones. a-e: tropical oceans, temperate oceans, Arctic Ocean, Southern Ocean, and Shelf Water (shown in Extended Data Fig. 5). Environmental variables and path coefficient descriptions are consistent with those presented in Fig. 3h.

https://doi.org/10.1038/s41558-025-02375-1

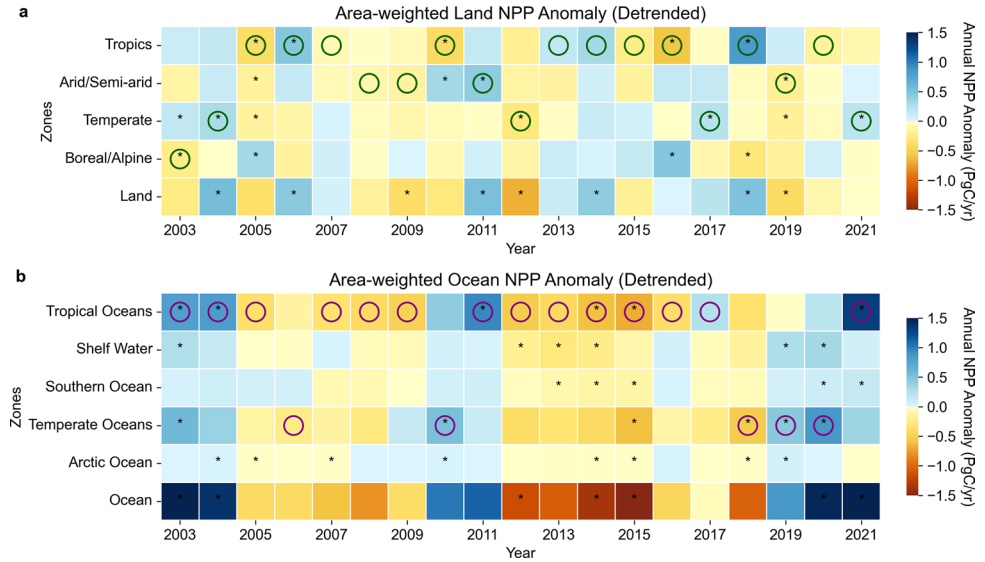

Extended Data Fig. 9 | Comparison of inter-annual variations in land and ocean NPP across different zones. a. Land zones. **b**, Ocean zones. Annual NPP anomalies are relative to the multi-year mean from 2003 to 2021. Annual NPP values are detrended, and anomalies are calculated relative to the 2003–2021 mean for each zone. The zone exhibiting the highest absolute anomaly each year is marked with green circles for land NPP (in **a**) and purple circles for ocean NPP (in **b**). Zonal NPP values with Z-scores (defined as the ratio of the annual anomaly to the multi-year standard deviation) greater than 1.0 are indicated with an asterisk (*). Land and ocean zones are shown in Extended Data Fig. 5.

https://doi.org/10.1038/s41558-025-02375-1

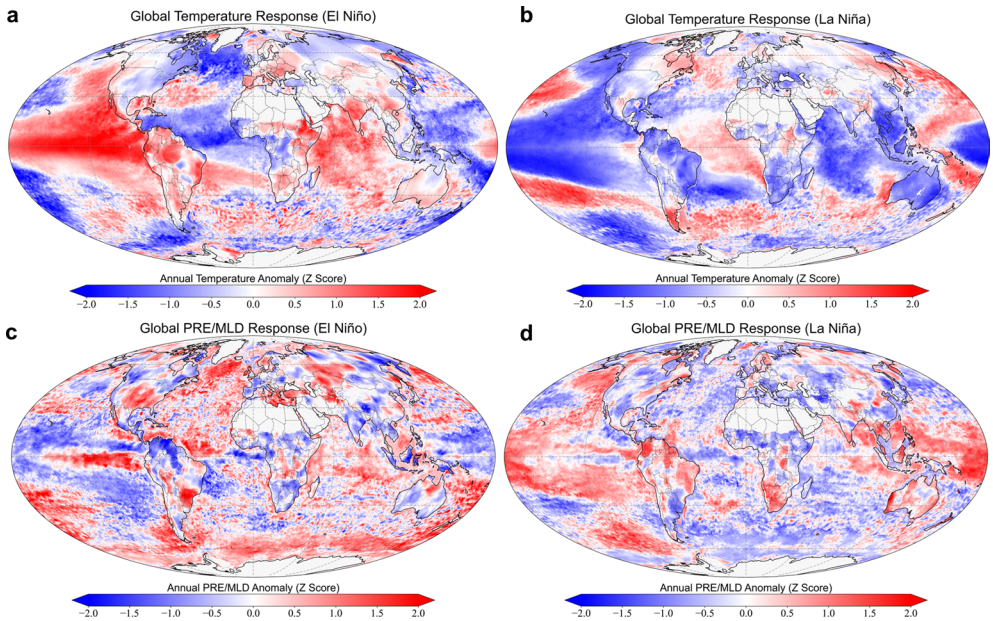

Extended Data Fig. 10 | Environmental responses during the identified strong El Niño and La Niña events. a, c, El Niño. **b, d**, La Niña. In **a** and **b**, land temperature represents the multi-year mean air temperature (TA), while ocean temperature refers to the multi-year mean sea surface temperature (SST) during the identified ENSO years. In **c** and **d**, land is represented by multi-year mean precipitation (PRE), and ocean is represented by multi-year mean mixed layer depth (MLD) during the identified ENSO years. All data are normalized as Z-scores, calculated by dividing annual anomalies by the multi-year standard deviation (2003–2021).

nature portfolio

Corresponding author(s): Yulong Zhang; Nicolas Cassar

Last updated by author(s): Jun 2, 2025

Reporting Summary

Nature Portfolio wishes to improve the reproducibility of the work that we publish. This form provides structure for consistency and transparency in reporting. For further information on Nature Portfolio policies, see our Editorial Policies and the Editorial Policy Checklist.

Statistics

For all statistical analyses, confirm that the following items are present in the figure legend, table legend, main text, or Methods section.

n/a	Confirmed	
☐	☒	The exact sample size (*n*) for each experimental group/condition, given as a discrete number and unit of measurement
☒	☐	A statement on whether measurements were taken from distinct samples or whether the same sample was measured repeatedly
☐	☒	The statistical test(s) used AND whether they are one- or two-sided *Only common tests should be described solely by name; describe more complex techniques in the Methods section.*
☒	☐	A description of all covariates tested
☒	☐	A description of any assumptions or corrections, such as tests of normality and adjustment for multiple comparisons
☐	☒	A full description of the statistical parameters including central tendency (e.g. means) or other basic estimates (e.g. regression coefficient) AND variation (e.g. standard deviation) or associated estimates of uncertainty (e.g. confidence intervals)
☐	☒	For null hypothesis testing, the test statistic (e.g. *F*, *t*, *r*) with confidence intervals, effect sizes, degrees of freedom and *P* value noted *Give P values as exact values whenever suitable.*
☒	☐	For Bayesian analysis, information on the choice of priors and Markov chain Monte Carlo settings
☒	☐	For hierarchical and complex designs, identification of the appropriate level for tests and full reporting of outcomes
☒	☐	Estimates of effect sizes (e.g. Cohen's *d*, Pearson's *r*), indicating how they were calculated

Our web collection on statistics for biologists contains articles on many of the points above.

Software and code

Policy information about availability of computer code

Data collection	We used the open-accessed FileZilla 3.5 and wget to batch downloading the data listed in Table S1.
Data analysis	We used the open-accessed Python 3.11 and Jupyter Lab 4.2.5 to conduct the data analysis. The codes for major analysis and for producing Figs. 1-4 are available in a OSF repository (https://doi.org/10.17605/OSF.IO/86K3N). Details of analysis were described in the Method section.

For manuscripts utilizing custom algorithms or software that are central to the research but not yet described in published literature, software must be made available to editors and reviewers. We strongly encourage code deposition in a community repository (e.g. GitHub). See the Nature Portfolio guidelines for submitting code & software for further information.

Data

Policy information about availability of data

All manuscripts must include a data availability statement. This statement should provide the following information, where applicable:

- Accession codes, unique identifiers, or web links for publicly available datasets
- A description of any restrictions on data availability
- For clinical datasets or third party data, please ensure that the statement adheres to our policy

All data needed to evaluate the conclusions in the paper are publicly available, with their respective access links provided in Table S1.

Human research participants

Policy information about studies involving human research participants and Sex and Gender in Research.

Reporting on sex and gender	N/A
Population characteristics	N/A
Recruitment	N/A
Ethics oversight	N/A

Note that full information on the approval of the study protocol must also be provided in the manuscript.

Field-specific reporting

Please select the one below that is the best fit for your research. If you are not sure, read the appropriate sections before making your selection.

☐ Life sciences ☐ Behavioural & social sciences ☒ Ecological, evolutionary & environmental sciences

For a reference copy of the document with all sections, see nature.com/documents/nr-reporting-summary-flat.pdf

Ecological, evolutionary & environmental sciences study design

All studies must disclose on these points even when the disclosure is negative.

Study description	We comprehensively explored annual trend and variability in global NPP from 2003 to 2021 using multiple satellite-derived NPP products for both land and ocean. We aimed to elucidate the patterns and drivers of contemporary global NPP trend and variability, with a particular focus on potential synergies and trade-offs between terrestrial and marine ecosystems.
Research sample	To facilitate our global analysis, we produced a land mask based on the 5km International Geosphere-Biosphere Programme MODIS land cover classification (MCD12C1 C61). Non-vegetated areas (urban, barren, permanent snow and ice and water bodies) were excluded based on the majority classification from 2003 to 2021. For the ocean mask, we excluded perennial sea ice areas with the multi-year mean NPP value lower than 0.01 gC/m2/yr. Inner freshwater lakes were omitted from our analysis due to high uncertainties in current ocean NPP products. For regional land analysis, we delineated four climate zones including tropical, arid/ semi-arid, temperate, and boreal/alpine, based on the 1-km Köppen-Geiger climate classification. The tropical zone is further subdivided into Tropical America, Tropical Africa and Tropical Asia based on the continent (Fig. S7A). Ocean analysis employed six zones including Pacific Ocean, Atlantic Ocean, India Ocean, Southern Ocean, Arctic Ocean and Shelf Water (Fig. S7B). The Shelf Water was derived from derived from Marine Ecoregions of the World (MEOW) and Pelagic Provinces of the World (PPOW), representing global coast and shelf areas where most of the human activity and conservation action are concentrated. The three major oceans (Pacific, Atlantic and Indian) were further categorized into tropical oceans (35°N to 35°S, including subtropical regions), northern temperate oceans (north of 35°N; not applicable for the Indian Ocean), and southern temperate oceans (south of 35°S).
Sampling strategy	All the global and zonal statistics (mean and total) are calculated by considering the area weight (caused by projection) and based on the spatially contiguous remote sensing and geophysical products shown in Table S1, thus representing the entire study regions.
Data collection	All data were downloaded through the open accessed URLs shown in Table S1. The open-accessed ftp tool FileZilla 3.5 and wget were used for batching downloading.
Timing and spatial scale	The original data were either daily, 8-day or monthly data from 2003 to 2021 at the global scales (crossing both land and ocean). The final analysis were aggregated at the annual scale with a spatial resolution of ~5km for land and ~8km for ocean during this period.
Data exclusions	No data were excluded in this analysis.
Reproducibility	Our analysis were based on the open-accessed remote sensing-based NPP product, geophysical data and well-defined methods, thus the results could be reliably reproduced.
Randomization	We conducted all the global and zonal statistics by considering all wall-to-wall pixels, thus randomization does not apply for our study.
Blinding	Our study relied solely on global gridded datasets without sample collection or selection, so blinding procedures were not applicable here.

Did the study involve field work? ☐ Yes ☒ No

Reporting for specific materials, systems and methods

We require information from authors about some types of materials, experimental systems and methods used in many studies. Here, indicate whether each material, system or method listed is relevant to your study. If you are not sure if a list item applies to your research, read the appropriate section before selecting a response.

Materials & experimental systems

n/a	Involved in the study
☒	☐ Antibodies
☒	☐ Eukaryotic cell lines
☒	☐ Palaeontology and archaeology
☒	☐ Animals and other organisms
☒	☐ Clinical data
☒	☐ Dual use research of concern

Methods

n/a	Involved in the study
☒	☐ ChIP-seq
☒	☐ Flow cytometry
☒	☐ MRI-based neuroimaging

Terms and Conditions

Springer Nature journal content, brought to you courtesy of Springer Nature Customer Service Center GmbH (“Springer Nature”).
Springer Nature supports a reasonable amount of sharing of research papers by authors, subscribers and authorised users (“Users”), for small-scale personal, non-commercial use provided that all copyright, trade and service marks and other proprietary notices are maintained. By accessing, sharing, receiving or otherwise using the Springer Nature journal content you agree to these terms of use (“Terms”). For these purposes, Springer Nature considers academic use (by researchers and students) to be non-commercial.
These Terms are supplementary and will apply in addition to any applicable website terms and conditions, a relevant site licence or a personal subscription. These Terms will prevail over any conflict or ambiguity with regards to the relevant terms, a site licence or a personal subscription (to the extent of the conflict or ambiguity only). For Creative Commons-licensed articles, the terms of the Creative Commons license used will apply.
We collect and use personal data to provide access to the Springer Nature journal content. We may also use these personal data internally within ResearchGate and Springer Nature and as agreed share it, in an anonymised way, for purposes of tracking, analysis and reporting. We will not otherwise disclose your personal data outside the ResearchGate or the Springer Nature group of companies unless we have your permission as detailed in the Privacy Policy.
While Users may use the Springer Nature journal content for small scale, personal non-commercial use, it is important to note that Users may not:

1. use such content for the purpose of providing other users with access on a regular or large scale basis or as a means to circumvent access control;
2. use such content where to do so would be considered a criminal or statutory offence in any jurisdiction, or gives rise to civil liability, or is otherwise unlawful;
3. falsely or misleadingly imply or suggest endorsement, approval , sponsorship, or association unless explicitly agreed to by Springer Nature in writing;
4. use bots or other automated methods to access the content or redirect messages
5. override any security feature or exclusionary protocol; or
6. share the content in order to create substitute for Springer Nature products or services or a systematic database of Springer Nature journal content.

In line with the restriction against commercial use, Springer Nature does not permit the creation of a product or service that creates revenue, royalties, rent or income from our content or its inclusion as part of a paid for service or for other commercial gain. Springer Nature journal content cannot be used for inter-library loans and librarians may not upload Springer Nature journal content on a large scale into their, or any other, institutional repository.
These terms of use are reviewed regularly and may be amended at any time. Springer Nature is not obligated to publish any information or content on this website and may remove it or features or functionality at our sole discretion, at any time with or without notice. Springer Nature may revoke this licence to you at any time and remove access to any copies of the Springer Nature journal content which have been saved.
To the fullest extent permitted by law, Springer Nature makes no warranties, representations or guarantees to Users, either express or implied with respect to the Springer nature journal content and all parties disclaim and waive any implied warranties or warranties imposed by law, including merchantability or fitness for any particular purpose.
Please note that these rights do not automatically extend to content, data or other material published by Springer Nature that may be licensed from third parties.
If you would like to use or distribute our Springer Nature journal content to a wider audience or on a regular basis or in any other manner not expressly permitted by these Terms, please contact Springer Nature at

onlineservice@springernature.com